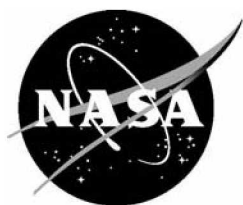


NASA/CR-2010-216709
NIA Report No. 2010-03



Assessment of Static Delamination Propagation Capabilities in Commercial Finite Element Codes Using Benchmark Analysis

Adrian C. Orifici
RMIT University, Melbourne, Victoria, Australia

Ronald Krueger
National Institute of Aerospace, Hampton, Virginia

June 2010

NASA STI Program . . . in Profile

Since its founding, NASA has been dedicated to the advancement of aeronautics and space science. The NASA scientific and technical information (STI) program plays a key part in helping NASA maintain this important role.

The NASA STI program operates under the auspices of the Agency Chief Information Officer. It collects, organizes, provides for archiving, and disseminates NASA's STI. The NASA STI program provides access to the NASA Aeronautics and Space Database and its public interface, the NASA Technical Report Server, thus providing one of the largest collections of aeronautical and space science STI in the world. Results are published in both non-NASA channels and by NASA in the NASA STI Report Series, which includes the following report types:

- **TECHNICAL PUBLICATION.** Reports of completed research or a major significant phase of research that present the results of NASA programs and include extensive data or theoretical analysis. Includes compilations of significant scientific and technical data and information deemed to be of continuing reference value. NASA counterpart of peer-reviewed formal professional papers, but having less stringent limitations on manuscript length and extent of graphic presentations.
- **TECHNICAL MEMORANDUM.** Scientific and technical findings that are preliminary or of specialized interest, e.g., quick release reports, working papers, and bibliographies that contain minimal annotation. Does not contain extensive analysis.
- **CONTRACTOR REPORT.** Scientific and technical findings by NASA-sponsored contractors and grantees.
- **CONFERENCE PUBLICATION.** Collected papers from scientific and technical conferences, symposia, seminars, or other meetings sponsored or co-sponsored by NASA.
- **SPECIAL PUBLICATION.** Scientific, technical, or historical information from NASA programs, projects, and missions, often concerned with subjects having substantial public interest.
- **TECHNICAL TRANSLATION.** English-language translations of foreign scientific and technical material pertinent to NASA's mission.

Specialized services also include creating custom thesauri, building customized databases, and organizing and publishing research results.

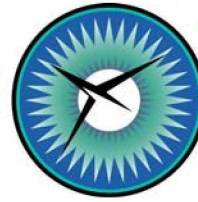
For more information about the NASA STI program, see the following:

- Access the NASA STI program home page at <http://www.sti.nasa.gov>
- E-mail your question via the Internet to help@sti.nasa.gov
- Fax your question to the NASA STI Help Desk at 443-757-5803
- Phone the NASA STI Help Desk at 443-757-5802
- Write to:
NASA STI Help Desk
NASA Center for AeroSpace Information
7115 Standard Drive
Hanover, MD 21076-1320

NASA/CR-2010-216709
NIA Report No. 2010-03



NATIONAL
INSTITUTE OF
AEROSPACE



Assessment of Static Delamination Propagation Capabilities in Commercial Finite Element Codes Using Benchmark Analysis

Adrian C. Orifici
RMIT University, Melbourne, Victoria, Australia

Ronald Krueger
National Institute of Aerospace, Hampton, Virginia

National Aeronautics and
Space Administration

Langley Research Center
Hampton, Virginia 23681-2199

Prepared for Langley Research Center
under Cooperative Agreement NNL09AA00A

June 2010

Trade names and trademarks are used in this report for identification only. Their usage does not constitute an official endorsement, either expressed or implied, by the National Aeronautics and Space Administration.

Available from:

NASA Center for Aerospace Information
7115 Standard Drive
Hanover, MD 21076-1320
443-757-5802

ASSESSMENT OF STATIC DELAMINATION PROPAGATION CAPABILITIES IN COMMERCIAL FINITE ELEMENT CODES USING BENCHMARK ANALYSES

Adrian C. Orifici¹, Ronald Krueger²

ABSTRACT

With the increasing implementation into commercial finite element (FE) codes of capabilities for simulating delamination growth in composite materials, the need for benchmarking and assessing these capabilities is critical. In this study, benchmark analyses were performed to assess the delamination propagation simulation capabilities of the VCCT implementations in Marc™ 2008r1 and MD Nastran™ R3 v2008.0 in solution sequences SOL 400 and SOL 600. Benchmark delamination growth results for Double Cantilever Beam (DCB), Single Leg Bending (SLB) and End Notched Flexure (ENF) specimens were generated using a numerical approach. This numerical approach was developed previously, and involves comparing results from a series of analyses at different delamination lengths to a single analysis with automatic crack propagation. Experimental and analytical benchmark delamination growth results were also taken from the literature for a second DCB specimen. Specimens were analyzed with three-dimensional and two-dimensional models, and compared with previous analyses using Abaqus® with the VCCT implemented. The results demonstrated that the VCCT implementation in Marc™ and MD Nastran™ was capable of accurately replicating the benchmark delamination growth results. The analyses in Marc™ and MD Nastran™ were significantly more computationally efficient than previous analyses conducted in Abaqus®. This was due to a lack of convergence issues, and a solution process that maintained the use of large time increments. The Marc™ and MD Nastran™ solvers encountered problems for some models with determining the appropriate crack growth direction, which required overriding the default automatic procedure. The results also demonstrated that the use of the numerical benchmarks was efficient and offers advantages over benchmarking using experimental and analytical results.

1. INTRODUCTION

One of the most common failure modes for composite structures is delamination [1-4]. To characterize the onset and propagation of delamination, the use of fracture mechanics has become common practice over the past two decades [1, 5, 6]. The strain energy release rate, G_T , is typically used as a measure of the driving force for delamination growth in composite laminates. Depending upon external loading conditions, G_T can be any combination of the three strain energy release rate components, G_I , G_{II} , and G_{III} , illustrated in Figure 1. The mode I component, G_I , arises from loading acting normal to the delamination plane, G_{II} arises from in-plane shear stresses acting perpendicular to the delamination front, and G_{III} arises from in-plane shear stresses acting parallel to the delamination front. To predict delamination onset or propagation, the total strain energy release rate is compared to the interlaminar fracture toughness, G_c , which is dependent on the relative proportions of the mode components. Due to the availability of test methods for characterizing mode I, II and mixed mode I/II delamination, efforts [7-9] have focused on evaluating the dependence of G_c on this range of mode mix. Such a quasi-static mixed-mode I/II fracture criterion

¹ RMIT University, GPO Box 2476, Melbourne, Victoria 3001, Australia.

² National Institute of Aerospace (NIA), 100 Exploration Way, Hampton, VA 23666, resident at Durability, Damage Tolerance and Reliability Branch, NASA Langley Research Center, MS 188E, Hampton, VA, 23681.

is determined by plotting G_c versus the mixed-mode ratio, G_{II}/G_T . The mixed-mode ratio is determined from data generated using pure mode I Double Cantilever Beam (DCB) ($G_{II}/G_T=0$), pure mode II End-Notched Flexure (ENF) ($G_{II}/G_T=1$), and Mixed-Mode Bending (MMB) tests of varying ratios. Examples are shown in Figure 2a for T300/914C and Figure 2b for C12K/R6376 [10, 11]. A curve fit of the data is performed to determine a mathematical relationship between G_c and G_{II}/G_T . [12, 13]. An interaction criterion incorporating mode III was recently proposed by Reeder [14]. Application of Reeder's 3D criterion is restricted due to the absence of a reliable means for measuring G_{IIIc} . Although, a standardized test for measuring this property is currently being investigated [15, 16], and several candidate specimens have been proposed in the literature [17, 18].

The virtual crack closure technique (VCCT) is widely used for computing energy release rates, based on results from continuum (2D) and solid (3D) finite element (FE) analyses, and to supply the mode separation required when using mixed-mode fracture criteria [19, 20]. The VCCT has been used mainly by scientists in universities, research institutions and government laboratories, and is usually implemented in their own specialized codes or used in post-processing routines in conjunction with general purpose FE codes. An increased interest in fracture mechanics to assess the damage tolerance of composite structures in design and certification has also renewed interest in the VCCT. As such, the VCCT has been implemented into the commercial FE codes Abaqus^{®1} [21] as well as MD Nastran[™] [22] and Marc^{™2} [23], among others. The implementation into the commercial FE code SAMCEF^{™3} [24] is a mix of the VCCT and the Virtual Crack Extension Method suggested by Parks [25].

As new approaches for analyzing composite delamination are incorporated into FE codes, the need for comparison and benchmarking becomes important. The implementation of technologies into FE codes involves numerical parameters, which can be unique to each code, and need to be understood and calibrated for any analysis. Experimental results used as benchmarks are valuable, but are complicated by aspects such as fiber bridging, crack branching, and experimental variance. Analytical results are also useful as benchmarks, but are not available for all specimen types and configurations, and can become complicated when dealing with aspects such as nonlinearity and three-dimensional (3D) effects. In response, a numerical benchmarking approach was developed in which results for delamination growth are first generated from a series of static analyses with different delamination lengths [26]. These benchmark results are then compared to simulation of delamination propagation using a single analysis. In previous work, this numerical benchmarking approach was applied to DCB and Single Leg Bending (SLB) specimens to assess the implementation of VCCT in Abaqus[®]/Standard [26].

In this study, the delamination propagation simulation capabilities of the commercial FE codes Marc[™] 2008r1 and MD Nastran[™] v2008.0 with the VCCT were assessed. Benchmark delamination growth results for DCB, SLB and ENF specimens were generated using a previously developed numerical approach [26]. Experimental and analytical benchmark delamination growth results were taken from the literature for a second DCB specimen [27]. Specimens were analyzed using two-dimensional (2D) plane strain and full 3D models and results were compared to previous analyses using Abaqus[®]/Standard with the VCCT implemented.

¹ Abaqus[®] is manufactured by Dassault Systèmes Simulia Corp. (DSS), Providence, RI, USA.

² MD Nastran[™], MSC Nastran[™], MSC Patran[™], Marc[™] and Mentat[™] are manufactured by MSC Software Corp., Santa Ana, CA, USA. NASTRAN[®] is a registered trademark of NASA.

³ SAMCEF[™] is manufactured by Samtech, Liège, Belgium.

2. SPECIMEN DESCRIPTION

For the current investigation, specimens were selected to investigate single mode (I and II) and mixed-mode I/II delamination growth with unidirectional and multi-directional laminates, using benchmark results from numerical and experimental studies. Two DCB specimens (labeled “DCB-1” and “DCB-2”), one SLB specimen and one ENF specimen were chosen, as shown in Figure 3, Figure 4 and Figure 5, respectively. The specifications for the DCB-1 and SLB specimens originated in previous work, in which experimental and numerical studies were performed and the critical strain energy release rates evaluated [28-31]. In this work, the DCB-1 and SLB specimens were selected as they were used to generate numerical benchmark delamination growth results previously [26]. The ENF specimen is the three-point bending 3ENF variant, and the specifications were set based on commonality with the DCB-1 specimen. The DCB-2 specimen (shown in Figure 3) was selected as benchmark experimental and analytical results were available in the literature [27]. The DCB and ENF specimens are used to determine the mode I and II interlaminar fracture toughness, G_{IC} [7] and G_{IIC} [9], respectively. The SLB specimen is used to evaluate the mixed-mode I/II interlaminar fracture toughness [30, 32].

The DCB-1 and ENF specimens consisted of T300/1076 graphite/epoxy with a unidirectional layup and the DCB-2 specimen consisted of T800/924 graphite/epoxy with a unidirectional layup. The SLB specimen used C12K/R6376 graphite/epoxy with a multi-directional layup of stacking sequence $[\pm 30/0/-30/0/30/0_4/30/0/-30/0/-30/30// -30/30/0/30/0/ -30/0_4/-30/0/30/0/\pm 30]$, where the double slash (//) denotes the location of the delamination. The material properties are given in Table 1. In general, mode I, mode II, and mixed-mode tests are performed on unidirectionally reinforced laminates where all fibers are aligned with the 0° direction. This means that delamination propagation occurs at a $[0/0]$ interface and delamination propagation is parallel to the fibers. Although this unidirectional layup is desired for standard test methods to generate fracture toughness data, delamination propagation between layers of the same orientation will rarely occur in real structures. Therefore, effects such as fiber bridging that are observed in DCB tests may not be present during mode I-dominated delamination growth between plies of dissimilar orientation.

3. METHODOLOGY

3.1 Fracture Criteria

Linear elastic fracture mechanics analysis of delamination in composite laminates involves determining the total strain energy release rate, G_T , and the individual components G_I , G_{II} and G_{III} , shown in Figure 1. The onset of delamination growth is predicted using the failure index:

$$\frac{G_T}{G_c} \geq 1 \quad (1)$$

where G_T is the sum of all mode components and G_c is the interlaminar fracture toughness. The fracture toughness is dependent on the relative proportions of the mode components, or the mode mix. A 2D relationship between G_c and modes I and II was suggested by Benzeggah and Kenane [13] and is given by:

$$G_c = G_{Ic} + (G_{IIc} - G_{Ic}) \left(\frac{G_{II}}{G_T} \right)^\eta \quad (2)$$

where G_{Ic} and G_{IIc} are determined experimentally from DCB tests [7] and ENF tests [9], respectively, and the 2D mixed-mode exponent η is determined from MMB tests of varying ratios of G_I and G_{II} [8]. Figure 2a and 2b show the determination of these parameters from experimental data for the materials applied in this work, where η was determined by a curve fit using the Levenberg-Marquardt algorithm in KaleidaGraph^{TM3} graphing and data analysis software [33].

Recently, Reeder [14] suggested a modification to Equation 2 that incorporates the mode III component, which is given by:

$$G_c = G_{Ic} + (G_{IIc} - G_{Ic}) \left(\frac{G_{II} + G_{III}}{G_T} \right)^\eta + (G_{IIIc} - G_{IIc}) \frac{G_{III}}{G_{II} + G_{III}} \left(\frac{G_{II} + G_{III}}{G_T} \right)^\eta. \quad (3)$$

As no standards currently exist for determining G_{IIIc} , or a mixed-mode exponent involving mode III, in this work G_{IIIc} was taken as G_{IIc} and η was taken as the value characterized from 2D mode I/II data as shown in Figure 2.

3.2 Virtual Crack Closure Technique

3.2.1 Theory

The VCCT [19, 20] is based on the assumption that the energy released in extending a crack by a small amount, Δa , is equivalent to the work necessary to close the crack to its original length. In an FE analysis using the VCCT, the three strain energy release rate components are calculated at a crack front node by

$$\mathbf{G} = \frac{\mathbf{F} \cdot \delta}{2A}, \quad (4)$$

where \mathbf{G} is the column vector of strain energy release rate components, \mathbf{F} consists of the forces at nodes along the delamination front, δ is a row vector that consists of the relative displacements of the node pairs behind each corresponding crack front node, and A is the surface area created by crack growth. Equation 4 requires the calculation of a local crack front coordinate system and modification to account for arbitrary element sizes. The VCCT is applicable for 2D or 3D analysis with linear and quadratic elements [20].

Previous investigations have shown that the VCCT results can be mesh-dependent for delaminations between two dissimilar solids, such as between plies of different orientation. This is due to the oscillatory nature of stresses in the vicinity of a crack front at a bi-material interface. To avoid mesh dependency issues, it is recommended to use consistent crack tip element lengths between analyses that are being compared. Further detail on this issue is provided in Reference [20]. In the current work, the finite element meshes were all based on those used in previous analyses [26], where mesh convergence studies had been conducted.

³ KaleidaGraphTM is manufactured by Synergy Software, Reading, PA, USA.

3.2.2 VCCT in Marc™

The VCCT is implemented into Marc™ as a procedure to determine the strain energy release rate distribution at a crack front [23]. This is done at a single node in a 2D model, or along a series of nodes in a 3D model. Multiple cracks can also be modeled. The user only needs to define the crack front nodes, and the solver determines the appropriate nodes, forces and areas to use for the crack growth calculation. This implementation follows the description given by Krueger [20], which accounts for a crack front of arbitrary shape.

For propagating a crack front, there are several options: growth by remeshing, where the local mesh around the crack tip is moved and the surrounding mesh is adapted; growth along element edges, where the elements at the crack front are disconnected by creating duplicate nodes and modifying the element connectivity; growth by releasing constraint, where a fixed contact or tie restraint is released. In the current work, only the latter approach was applied, as this was the only approach that could be used with 3D solid elements.

For crack growth by releasing constraints, the user defines two surfaces that are initially bonded with a “glued” [23] constraint, or a set of multi-point constraints (MPCs) between nodes across an interface. In the current work, the contact-based approach was used, which is similar to the approach implemented within Abaqus® [21]. It is possible to define a completely bonded interface, and then to select certain nodes that are unbonded, or have the bond function “deactivated” [23], so that a pre-crack can be modeled. An example of this is shown in Figure 6, where a specimen with a pre-crack (shown in Figure 6a) is modeled using only a bonded interface (shown in Figure 6b), or with a combination of a bonded and unbonded contact interface (shown in Figure 6c).

At the end of every nonlinear analysis increment, the strain energy release rates are calculated using the VCCT. Crack growth onset is detected using Equation 1, with either single-mode or mixed-mode criteria for G_c . For single-mode criteria, three equations are used to consider each mode independently, and for mixed-mode, the Reeder (Equation 3) or Power law criteria are available [14]. The crack is “grown” by releasing the constraint at the crack front node, which extends the crack to the next node in the bonded contact region. If crack growth is detected at the end of the increment, the appropriate nodes are released, and the increment is restarted. Restarting the increment is repeated until Equation 1 is no longer satisfied at any crack front node, and is a critical step in ensuring that enough crack growth occurs within an increment. This aspect is detailed further in the Discussion section.

Another aspect that can become important is the way in which the VCCT algorithm locates the most appropriate node in the intact region to “grow” the crack, once propagation has been detected at a crack front node. In Marc™, this is based on the definition of the crack growth direction, where once this direction is determined, the solver will select the closest appropriate node from those available in the intact region. The default option in Marc™ is an automatic determination of the crack growth direction based on a maximum principal stress criterion, which defines the crack growth as being normal to the direction of greatest tension [23]. There are other options for specifying the crack growth direction that the user can select instead of the default, where the growth direction is instead aligned with either the most critical mode, with the mode I component, or with a fixed user-defined vector. The effect of this option is discussed further in the results for each specimen, and further detailed in the Discussion section.

3.2.3 VCCT in MD Nastran™ SOL 400

The VCCT is implemented into MD Nastran™ solution sequence SOL 400, and follows the same general approach as outlined above for Marc™. The SOL 400 solution sequence is an integration of the traditional nonlinear solver (SOL 106) with advanced nonlinear technologies [23]. This includes functionality developed originally in Marc™, such as contact and the VCCT technology for crack growth modeling. Critically though, not all aspects of the Marc™ implementation within a given software version are available in the MD Nastran™ version of the same release date [23, 22, 34]. As a key example of this limitation, in the SOL 400 version applied in this work (version 2008.0), the VCCT technology did not incorporate mixed-mode crack growth. Another important example is that only the default option for determining the crack growth direction could be specified as input.

3.2.4 VCCT in MD Nastran™ SOL 600

The VCCT is available in MD Nastran™ solution sequence SOL 600. The SOL 600 solution sequence is a “wrapper” application for Marc™, in which the user generates an MD Nastran™ input file, and the solver converts this into a Marc™ input file, runs the analysis natively in Marc™, and translates the Marc™ output into MD Nastran™ format [22]. However, despite running Marc™ natively, this solver can be limited by the translation process, which includes options available in Marc™ not being easily available within the MD Nastran™ input format, and some difficulties in “mapping” functionality between the two codes. As with the SOL 400 solver, a key example of the limitations of the SOL 600 solver in the version applied in this work was that the VCCT technology did not incorporate mixed-mode crack growth, and could only be used with the default option for determining the crack growth direction. While the SOL 400 solution sequence is exclusive to the MD Nastran™ analysis package, the SOL 600 solution sequence is also available within MSC Nastran™. As such, references made in this work to MD Nastran™ SOL 600 are identically applicable to MSC Nastran™ SOL 600.

4. FINITE ELEMENT MODELING

Typical 2D and 3D FE models of the DCB, SLB and ENF specimens are shown in Figure 7 to Figure 9, which also illustrates the boundary conditions applied for these models. The models were based on those presented previously [26]. An additional ENF model with a refined mesh was generated, which is shown in Figure 10 with boundary conditions, and discussed further in the results section. All models are summarized in Table 2, which lists the analysis solver and dimension (2D or 3D) for each model, with a reference to the corresponding mesh.

Along the specimen length, all models were divided into various sections with different mesh refinement. Although the dimensions of the elements varied, all meshes were based on a refined mesh region that used elements of 0.5 mm length in the crack growth direction in the region immediately around the delamination front. This element length was selected in previous studies [28, 31], in which mesh convergence investigations were performed. All models used a uniform mesh across the width direction. The specimens with unidirectional laminates used six elements through the specimen thickness ($2h$), while the multi-directional laminate specimens used a refined mesh based on a ply level mesh refinement around the delamination interface, as shown in Figure 8. Elements away from the delamination interface used a smeared material property for each sublaminates based on the rule of mixtures. Further detail and justification of the modeling is given in Reference [26].

For all models, the plane of delamination was modeled as a discrete discontinuity in the center of the specimen. To create the discrete discontinuity, each model was created from separate meshes for the upper and lower part of the specimens with identical nodal point coordinates in the plane of delamination. Two surfaces (top and bottom) were created on the meshes as illustrated in Figure 6, and a bonded (glued) contact specified between them. For the DCB and SLB specimens, the pre-crack was not included in the contact definition as no interaction between the two surfaces in this region was expected. For the ENF specimens, contact was required across the pre-cracked interface, so the entire surface was included in the bonded contact, and the pre-cracked region was created by deactivating the bonded contact for some nodes. For models that were analyzed without crack propagation (calculation of strain energy release rate only) as part of developing benchmark results as described later, the crack propagation capability was turned off.

The delaminated surfaces of the DCB and SLB specimens do not come into contact during their respective deformation, and thus unbonded contact was not necessary when analyzing these specimens. Avoiding the use of contact modeling is advantageous, as the inclusion of a contact algorithm significantly increases the solution time of an analysis. In these cases, only bonded contact was required in order to simulate delamination growth. The ENF specimen on the other hand does involve contact of the delaminated surfaces during deformation, and so unbonded contact was necessary to ensure that these surfaces did not interpenetrate during an analysis.

All specimens were analyzed with 3D models. Additionally 2D models of the DCB and ENF specimens were created. A summary of all models run in the current work is presented in Table 2. The 3D models used 8-node reduced integration solid brick elements (Marc™ element type 117 [23] and MD Nastran™ element type CHEXA [22]). The 2D models used two-dimensional 4-node plane strain elements (Marc™ element type 11 and MD Nastran™ element type CQUAD4). The 2D and 3D models for a specimen used the same mesh scheme, as shown in Figure 7 and Figure 9. The nonlinear solvers in Marc™ and MD Nastran™ were used, which applied a full Newton-Raphson solution procedure with a load residual tolerance of 0.001. The specimen loading was defined in terms of applied displacements, to minimize problems with numerical stability of the analysis caused by the unstable propagation. All models were run on a 32-bit Intel Core 2 Duo 2.25 GHz CPU processor.

Comparing codes, the input requirements for the VCCT analysis were the same, except for the lack of mixed-mode parameters in SOL 400 and SOL 600 as previously discussed. Details on the specific keywords and parameters required for a VCCT analysis in each code are given in the Appendix. The differences between the codes in terms of the more practical aspects of the application are detailed in the Discussion section.

5. ANALYSIS

5.1 Computation of Strain Energy Release Rates

For each of the specimens, the computed strain energy release rate distribution across the delamination front was plotted versus the normalized specimen width, y/B , as shown in Figure 11 to Figure 13, for the 3D and 2D models. Distributions were calculated for a range of different delamination lengths, as part of the numerical benchmark results generation described in the next section. As strain energy release rate distributions for different delamination lengths were previously presented for the DCB and SLB specimens [26], the results in Figure 11 and Figure 12, respectively, are given for only one delamination length. The ENF results in Figure 13 are given for all delamination lengths investigated, for the same applied displacement. For the DCB and ENF specimens, only the dominant mode component is shown (I and II respectively), as the others were

negligible, and there was no 2D model for the SLB specimen. For the DCB and SLB specimens, Figure 11 and Figure 12 demonstrate the excellent agreement between the results in Marc™ and those calculated using Abaqus® in previous work [26]. The results for all specimens demonstrate that due to 3D effects, such as anticlastic bending of the loading specimen arms, the strain energy release rate distribution was non-constant across the delamination front, even for single-mode dominated specimens. These curved distributions can cause an initial straight front to grow into a curved front. This process has been observed both analytically and experimentally [26, 35-39].

For the ENF specimen, the results in Figure 13 show that the strain energy release rates initially increased with increasing delamination length, which would cause unstable delamination growth. This trend changed with respect to the location of the central loading pin, which corresponds to a delamination length of 70 mm. The average strain energy release rate initially decreased with an increase in delamination length, up to a maximum length corresponding to the loading pin location, and then began to increase with longer delamination lengths. This suggests that crack growth at delamination lengths past the loading pin was stable. From the results in Figure 13, it was found that the distribution of G_{II} across the delamination front changed slightly with delamination length. In this case, G_{II} peaks on the edges of the delamination front at shorter delamination lengths, and peaks in the center at longer delamination lengths. The distribution also becomes more curved at delamination lengths approaching the loading pin. The unstable nature of delamination growth in ENF specimens loaded quasi-statically, under displacement control, is well documented in the literature [40-42].

5.2 Creating Benchmark Delamination Growth Results

The approach developed previously for generating numerical benchmark delamination growth results [26] was applied to the DCB-1, SLB and ENF specimens. For these specimens, a benchmark result set was extracted from a series of models with different delamination lengths. These models did not simulate delamination propagation, and were only used to get the load-displacement response and the strain energy release rate distribution for different delamination lengths. For each delamination length modeled, a failure index was calculated across the delamination front using Equation 1, with the Reeder mixed-mode criterion used to compute G_c (Equation 3). Delamination growth onset was assumed when the failure index at the center of the specimen ($y/B = 0$) reached a value of unity. Specimen load-displacement response up to this point was also assumed to be linear. Subsequently, the displacement and load at delamination growth onset, δ_{crit} and P_{crit} respectively, was computed by linearly scaling the prescribed displacement and load in each analysis (δ and P respectively), using the following relations [26]:

$$\frac{G_T}{G_c} = \frac{P^2}{P_{crit}^2} \Rightarrow P_{crit} = P \sqrt{\frac{G_c}{G_T}}, \quad \delta_{crit} = \delta \sqrt{\frac{G_c}{G_T}}, \quad (5)$$

The benchmark result set is constructed by plotting the displacement at delamination growth onset versus delamination length, as illustrated in Figure 14 for the DCB-1 specimen. This form is used for the benchmark result because all specimens were loaded via a prescribed displacement, and the change in delamination length is the most appropriate output for assessment of delamination growth. In previous work [26], the benchmark results were presented as load-displacement curves, to illustrate the application of Equation 5.

The benchmark delamination growth results for the DCB-1, SLB and ENF specimens are presented in Figure 14, Figure 15 and Figure 16, respectively. Results from previous analyses with Abaqus® [26] are also included for the DCB-1 and SLB specimens. The DCB-1 results show that the applied opening displacement increased with increasing delamination length, which indicates stable growth under displacement control. In contrast, both the SLB and ENF results indicate initial unstable delamination growth, as the critical displacement decreases with increasing delamination length. The comparison between the Abaqus® and Marc™ results in Figure 14 and Figure 15 shows that the two solvers gave almost identical results for these models.

5.3 Delamination Propagation Analysis: DCB-1

For the DCB-1 specimen, the previous results in Figure 14 show that delamination propagation was predicted to initiate at an applied opening displacement ($\delta/2$) of 0.75 mm. Based on this, a two-step loading procedure was applied for the delamination propagation analysis, which involved using coarse time increments until just before failure, and fine increments for the region involving delamination propagation. Dividing the first step into relatively coarse time increments was possible as the load-displacement behavior of the specimen up to failure was expected to be linear. In the first step, a prescribed opening displacement of $\delta/2 = 0.7$ mm was applied in 10 increments. In the second step, the total prescribed displacement was increased to $\delta/2 = 1.0$ mm. This was applied with a fixed time increment scheme of 50 increments ($\delta/2 = 0.006$ mm each increment).

In both Marc™ and MD Nastran™, the solver has the capability to cut back the increment size in the event of convergence issues. In addition, the Marc™ solver has the capability to activate damping when the time step is reduced below a defined minimum. Critically, no convergence issues were seen throughout any analyses, and damping was not required. This is quite different behavior from that seen previously with Abaqus® [26], where convergence issues associated with delamination growth caused significant cutbacks in the time increment, required investigation of suitable damping parameters and involved an increase in computational expense. As a result, run times for delamination propagation analyses were within a minute for the 2D models and generally within a few hours for the 3D models, depending on the selection of increment size and amount of delamination growth. The efficiency of the solver is discussed further in a later section.

The DCB-1 specimen was analyzed with Marc™, MD Nastran™ SOL 400 and MD Nastran™ SOL 600, with both 2D and 3D models, as shown in Table 2. All solvers detected delamination propagation using simple single-mode criteria, as the SOL 400 and SOL 600 solvers did not have any mixed-mode criteria as previously discussed. The results of all analyses are shown in Figure 17 to Figure 19, where Figure 17 to Figure 18 are the results from only the Marc™ analysis, and Figure 19 is a comparison of the delamination growth results from all solvers.

From the delamination growth results in Figure 17, the VCCT technology gave very close comparison with the benchmark results, for both 2D and 3D models. The 3D models showed delamination growth at slightly lower applied displacements, which was due to the slightly higher strain energy release rates in the 3D models as shown in Figure 11.

From Figure 18, the delamination was seen to propagate as a straight crack front, which contradicts the curved strain energy release rate distribution shown in Figure 11. This propagation of a straight front is related to the coarse element size and was also seen in previous analyses [26, 43].

From Figure 19, all solvers produced almost identical results, for both 2D and 3D models. This indicates that the implementation of the VCCT technology is common across solvers. The only

discrepancy of note was seen for the 3D model, where on two occasions the SOL 400 model showed delamination growth an increment earlier than the Marc[™] and SOL 600 models. This can be seen in Figure 19 for the first and last delamination growth increments shown (at $\Delta a = 0$ mm and $\Delta a = 4.5$ mm). This was attributed to slight numerical differences between the solvers.

The characteristic step pattern seen in the delamination growth results in Figure 17 and Figure 19 was caused by the step change in length as the delamination was grown one element length at a time. In the case of the 3D models, the delamination was seen to propagate across the crack front within the same increment. This step pattern is illustrated in Figure 20, where the numbered stages show the initial increase in applied displacement (1-2), sudden nodal release (2-3), increase in displacement until next delamination growth (3-4), and repetition (4-5, 5-6, etc.). These step changes in delamination length at a fixed applied displacement would produce a sequence of drops in the reaction load and the corresponding “saw-tooth” pattern in the load-displacement response [43, 44]. The results also show that the corners of the steps, just before a delamination growth event, provide the most suitable comparison with the benchmark results, which also allows coarse meshes to be adequately used.

5.4 Delamination Propagation Analysis: DCB-2

For the DCB-2 specimen [27], the analysis used the model shown in Figure 7, with the width across the delamination front increased from 25 mm to 30 mm. The analysis used two load steps with coarse and fine time step incrementation, as discussed for the DCB-1 specimen. In the first step, a prescribed displacement of $\delta/2 = 0.9$ mm was applied in 2 increments, while in the second step the total prescribed displacement was increased to $\delta/2 = 6.0$ mm in 250 increments ($\delta/2 = 0.0204$ mm each increment). As with the DCB-1 specimen, no significant convergence issues were seen and damping was not required.

The DCB-2 specimen was analyzed in Marc[™] with both 2D and 3D models as shown in Table 2. Delamination propagation was detected using single-mode criteria. Numerical results were also taken from a previous publication [45], in which the DCB-2 specimen was analyzed using Abaqus[®] 6.8. Further detail on the modeling approach adopted in that work is given in References [21, 26, 45], which includes discussion on the damping and other parameters required. Benchmark analytical solutions for delamination growth were taken from Reference [27], where relationships between the applied displacement and delamination length are presented based on beam theory. Experimental delamination growth results were taken from Reference [46], where the delamination length was measured at intervals on the edge of the specimen. The experimental results were included since the original experiments showed very little fiber bridging [46], which is not accounted for in the analysis. The delamination growth results of all analyses and benchmarks are shown in Figure 21.

It is observed from Figure 21 that the VCCT technology was capable of accurately representing the analytical and experimental benchmark results in terms of delamination growth behavior. Excellent agreement was seen between the two analysis codes, and between the numerical analyses and both the experimental and analytical results. The change in character of the Marc[™] results at a delamination growth $\Delta a = 40$ mm was due to the delamination reaching a region of the mesh with larger elements, which led to larger step changes in delamination growth. At the transition between the fine and coarse mesh regions, the Marc[™] results showed a deviation from the expected behavior. As discussed previously for the DCB-1 specimen and illustrated in Figure 20, the peak displacements just prior to delamination propagation in each step give a consistent

alignment with numerical benchmark results. The results at the mesh transition region indicated in Figure 21 demonstrate an error in the VCCT implementation, caused by the difference between element lengths ahead and behind the delamination front. The Abaqus® results shown in Figure 21 do not show this error since a consistently fine mesh was used. However, this error was seen in other Abaqus® results [45], and indicates a similar implementation error in both codes. The issue of mesh transition is further investigated and discussed in detail in Section 6.1.

The results for the DCB-2 specimen demonstrate the difference between code benchmarking using experimental and analytical approaches, in comparison with the use of the numerical benchmark results for the DCB-1. The use of experimental and analytical results is highly valuable in validating that the simulation is capable of capturing the physical phenomena. These approaches, however, may introduce additional factors that can influence an assessment of simulation capabilities, which include statistical variance, the use of approximations, or complications such as fiber bridging. As these aspects were not expected to be significant in this work, the comparisons with benchmark results for the DCB-1 and DCB-2 specimens produced similar conclusions. Further, the results for the two specimens demonstrate that numerical benchmarks are suited for efficiently isolating and assessing code capabilities as they involve a direct comparison between the behavior of identical models. The use of numerical benchmarks would also be highly valuable where experimental and analytical results are unavailable or difficult to obtain, such as for complex specimens and structures.

5.5 Delamination Propagation Analysis: SLB

For the SLB model, shown in Figure 8, the analysis used two load steps with coarse and fine time step incrementation as discussed for the DCB-1 specimen. In the first step, a prescribed center displacement of $w = 3.0$ mm was applied in 6 increments, while in the second step the total prescribed displacement was increased to $w = 4.0$ mm in 100 increments ($w = 0.01$ mm each increment). As with the DCB specimens, no significant convergence issues were seen and damping was not required.

One aspect that was critical for the analysis of the SLB specimen was that the crack growth direction needed to be specified with a user-defined vector, instead of with the default automatic algorithm that, as previously discussed, is based on a principal stress criterion. In preliminary SLB models using the default approach, errors were found in the propagation of the delamination front, where the solver would detect the critical node but not be able to locate the appropriate node in the intact region to grow the delamination front. This was found to be due to the calculated crack growth direction, which in some instances pointed in directions from which no suitable nodes could be found. This problem was also found to be particularly critical for edge nodes, and was found to occur for both coarse and fine meshes. In instances where the delamination could no longer be propagated due to the inappropriate crack growth direction, the entire delamination was made “inactive”, and all VCCT calculations were ceased.

In order to address this problem, it was necessary to specify a user-defined vector for the crack growth direction, which was possible for the SLB specimen, as the crack growth direction was known. For the SLB specimen as shown in Figure 8, the crack growth direction was aligned with the global x -direction (i.e. the user-defined crack growth direction vector was set to $\langle 1,0,0 \rangle$). It should be stated that the calculation of the strain energy release rates is not based on the crack growth direction, but uses a local crack front coordinate system as previously described. As such, setting the crack growth direction to be fixed acts only to assist the solver in locating the correct node for crack propagation, and does not influence the mode mixity at the crack front.

The consequence of this issue was that SOL 400 and SOL 600 could not be used to analyze the SLB specimen, as only the default crack growth direction option was available to be selected in the version of MD Nastran™ applied in this work. More critically, the SLB specimen is a mixed-mode problem, so that in any event, as only single-mode crack growth could be implemented, SOL 400 and SOL 600 could not have been used.

The SLB specimen was analyzed in Marc™ with a 3D model as shown in Table 2. Delamination propagation was detected using the Reeder mixed-mode criterion. A 2D model was not analyzed, as the multi-directional laminate could not be modeled correctly. The delamination growth results are shown in Figure 22, and the progression of the delamination front is illustrated in Figure 23.

From these results, the VCCT technology was again capable of accurately representing the delamination growth benchmark results for this mixed-mode case as shown in Figure 22. The benchmark results show that the SLB specimen exhibited an initial period of unstable delamination growth. This was caused by the strain energy release rates remaining critical with increasing delamination length. In the benchmark curve, unstable delamination growth is indicated by a reduction in applied displacement below the initiation point. As the analysis was run in displacement control, it was not possible to get a reduction in displacement, so the unstable delamination growth is seen as a large crack growth step. This corresponded to the delamination extending by 21 mm within one increment, which is shown in both Figure 22 and Figure 23. This was followed by stable delamination growth, where the benchmark and FE results correlated very closely. The delamination growth behavior as shown in Figure 23 demonstrated that a curved delamination front developed and propagated. This was caused by the curved strain energy release rate distribution as shown in Figure 12. As described for the DCB-1 specimen, this led to a slight difference compared to the benchmark results, which were generated based on a straight delamination front. It is possible that the exact shape of the delamination front shown in Figure 23 was affected by the delamination propagating through a mesh transition, which is further demonstrated for the ENF specimen and investigated in detail in the Discussion section.

5.6 Delamination Propagation Analysis: ENF

For the ENF model shown in Figure 9, the analysis used two load steps with coarse and fine time step incrementation as discussed for the DCB-1 specimen. In the first step, a prescribed center displacement of $w = 4.0$ mm was applied in 2 increments, while in the second step the total prescribed displacement was increased to $w = 8.0$ mm in 100 increments ($w = 0.04$ mm each increment). As with all previous specimens, no significant convergence issues were seen and damping was not required. However, as found for the SLB specimen, the default crack growth direction algorithm resulted in delamination propagation errors, and a user-defined vector was used. Again, due to the requirement for a user-defined crack growth vector, MD Nastran™ SOL 400 and SOL 600 could not be used.

The ENF specimen was analyzed in Marc™ with both 2D and 3D models as shown in Table 2. Delamination propagation was detected using single-mode criteria. The results of the analyses are shown in Figure 24 and Figure 25. As observed from these results, the VCCT technology was capable of accurately representing the benchmark delamination growth results for the baseline ENF mesh. As with the DCB-1 specimen, delamination growth was initiated in the 3D model at a slightly lower applied displacement than the 2D model, which was due to a slightly higher strain energy release rate as shown in Figure 13 for $a = 30$ mm.

The results for the ENF specimen showed initial unstable delamination propagation followed by stable propagation, in the same way as described for the SLB specimen. The first delamination growth event corresponded to a delamination growth step of 41 mm, as shown in Figure 24. The unstable delamination growth was followed by stable growth, where the benchmark and FE results correlated very closely. As previously discussed, the change from unstable to stable delamination growth is associated with the inflection point of the applied displacement versus delamination growth behavior, which is indicated in Figure 24. Although in experimental testing focused on material characterization, the delamination is not extended past this point, for the numerical analysis this region remains valuable for benchmarking purposes.

From Figure 25, the delamination front formed in the baseline mesh by the unstable delamination growth was jagged and non-straight across the width. This irregular and unexpected pattern was considered a product of the delamination propagating through a mesh transition region, in addition to insufficient mesh density across the width. A refined model, shown in Figure 10, was analyzed in which the delamination propagation only occurred in the fine mesh region, where the element length was 0.5 mm in the crack growth direction. Rather than using a large fine mesh region to capture all of the unstable delamination growth from $a = 30$ mm to $a = 71$ mm, it was decided to instead increase the length of the initial delamination to 65 mm. This located the delamination within the unstable delamination growth region, so that the stable delamination growth behavior would still be identical to the baseline case, while keeping the model size reasonable. Additionally, the mesh density across the width was doubled, while for efficiency the length of the fine mesh region was reduced.

The results of the analysis of the ENF refined mesh model are shown in Figure 26, where the increased mesh density and initial delamination of 65 mm produced a straight delamination front without the jaggedness across the width. The delamination growth results for the models are shown in Figure 27, where the initial delamination length of $a = 65$ mm is represented as a delamination growth $\Delta a = 35$ mm, so that the baseline for delamination growth in the two numerical analyses is the same. From the delamination growth results, it can be seen that despite different delamination front patterns, the models gave very close comparison with the benchmark curve for the stable delamination propagation stage. These results demonstrate that crack propagation through a mesh transition region could lead to an incorrect delamination front developing and propagating, and that the mesh refinement level was critical to accurately capturing the shape of the delamination front. The results in Figure 27 also clearly demonstrate the effect of large elements on the delamination growth, where the peaks of the large steps just prior to delamination growth gave the most suitable comparison with the benchmark results.

6. DISCUSSION

6.1 Mesh transition

The results in Figure 21 and Figure 25 demonstrated an error in the implementation of the VCCT in Marc[™], with regards to calculation of strain energy release rates, where elements ahead and behind the delamination front had different lengths. This was also seen for the Abaqus[®] solver in Reference [45]. As detailed in References [19, 20], the VCCT equations require a modification factor to account for uneven element lengths ahead and behind the crack front. The results in Figure 21 and Figure 25 demonstrate that this has not been implemented, so that uneven element lengths, such as those seen as a crack propagates through a mesh transition region, result in incorrect calculation of the strain energy release rate. To illustrate this effect further, a 2D DCB-1 model with

several mesh transition regions was analyzed in Marc[™], with the mesh and the results shown in Figure 28. The errors are most clear for the transition to smaller elements, as is shown at $\Delta a = 5.25$ mm, where an under-estimation of the strain energy release rates due to the mesh transition prevents delamination growth from occurring and following the benchmark results. The same error is less evident though still occurring in the two transitions to larger meshes at $\Delta a = 1.0$ mm and $\Delta a = 7.25$ mm. For the 2D DCB-1 model in this example, the errors did not propagate, so that predictions in a regular mesh following a mesh transition region returned to follow the benchmark solution. However, the results for the 3D ENF model demonstrated that an incorrect delamination front could develop due to a mesh transition region and be propagated.

6.2 Solver comparison: Marc[™] and Abaqus[®]

Comparing Marc[™] results in this work (which includes the adaptation of the Marc[™] implementation into MD Nastran[™]) with previous Abaqus[®] results [26], one clear difference was the solution process. Critically, in the Marc[™] implementation of VCCT [23], once crack growth is detected in an increment the crack front node is released and the increment is restarted. This allows for multiple crack growth instances to occur in one increment, and allows for coarse time increments to be used, which is computationally efficient. By comparison, in the Abaqus[®] implementation [21], only one crack growth instance can occur in each increment, so it is necessary to reduce the increment size considerably in order to ensure that no over-estimation occurs. The failure index determined from the strain energy release rates is monitored, and the user defines a limit on the amount that the failure index can exceed a value of 1.0. This overshoot limit, or “release tolerance”, as such becomes another parameter in the model that requires careful selection [26]. So, while the Abaqus[®] approach decreases the increment size to suit the crack growth, in Marc[™] the crack growth is increased to suit the increment size, so that larger increments can be used with increased computational efficiency.

The convenience of using large increments needs to be managed carefully with the need to capture the initiation point for crack growth. This is illustrated in Figure 29, where a DCB-1 specimen is analyzed in Marc[™] with fine and coarse time incrementation. With fine time increments, a step pattern of crack growth is observed, which indicates that no over-estimation is occurring due to the increment size. The analysis with coarse time increments is seen to follow the fine solution closely, though the use of coarse increments means that the exact initiation point for crack growth is not captured. This issue can be addressed by using different time incrementation throughout the analysis, where for example coarse increments are used until just before crack growth initiation (which could be determined from a preliminary coarse analysis), fine increments are used to capture the crack growth initiation, and if necessary coarse increments can be re-used to capture crack propagation. This is similar to the two-step approach applied in this work. Alternatively, it may be considered that the benefit of using coarse increments outweighs the slight increase in accuracy in capturing the initiation point, which may be more appropriate for analysis of large structures.

Another important difference between Marc[™] and Abaqus[®] is the convergence difficulties and the subsequent damping required. In previous work using Abaqus[®] [26], it was found that damping, or “stabilization”, needed to be added to the solver, in order to get a solution in light of the convergence issues. The introduction of stabilization parameters requires considerable effort in parametric investigation in order to determine a suitable compromise between damping and solution accuracy. In contrast, for the models considered in this work with Marc[™], no severe convergence issues were recorded and damping was not applied in any of the solutions.

The two aspects of differing time increment requirements (caused by allowing multiple crack growth events in an increment) and the requirement for damping meant that the Marc[™] solver was considerably more computationally efficient than the Abaqus[®] solver for the models analyzed. This was most noticeable for the 3D models, where for example, the Abaqus[®] solver required run times of up to several days [26], while the Marc[™] solver experienced run times of only several hours. Although the analyses were run on different machines, the comparison clearly highlights the considerable difference between the two solvers. This difference is further exacerbated by the introduction of the release tolerance and stabilization parameters in Abaqus[®], which typically require parametric investigations to determine.

One aspect that required attention in the Marc[™] analysis was the definition of the crack growth direction, where the default automatic algorithm was unable to propagate the crack correctly. With the user-defined vector, it was possible to achieve the correct solution for the problems considered. However, for problems where the crack growth direction is unknown or changes along the delamination front, this may present further difficulties. While information on the exact procedure implemented in Abaqus[®] is not available in the documentation, none of the previous analyses of DCB and SLB specimens indicated any issues with locating the correct nodes for crack propagation [26, 45].

The use of the crack growth direction in Marc[™] is an important difference from the implementation in Abaqus[®], and has both advantages and disadvantages. In Abaqus[®], the crack front node is simply “released” from contact, and the new crack front is found by determining which nodes lay on the boundary of the contact definition. This is a simple technique that ensures that there are no issues with propagation in terms of locating the correct nodes, which are located implicitly. In Marc[™], the use of the crack growth direction as a search vector is disadvantageous, as it introduces the possibility that either incorrect nodes are found, or no nodes are found at all. The difficulty in determining the correct crack growth direction is likely to be caused by the application of the principal stress criterion, where the accuracy of this criterion at the interface between two different orthotropic materials is uncertain, as the method was originally developed for isotropic metals.

On the other hand, the use of the crack growth direction in Marc[™] has the advantage of allowing the crack growth to be explicitly tracked for each node. As the crack front moves from one node to another, information regarding the accumulated crack growth is directly passed between nodes. In this way, each crack front node at any increment maintains the total crack growth it has taken for the crack to reach that node since the beginning of the analysis. This makes it very easy to track the crack growth at each node across the crack front, and also to implement R-curve behavior where the fracture toughness parameters vary with crack length.

Despite the advantages in explicitly tracking the crack growth data, it is possible to achieve a determination of the total crack growth for any node and a capacity to implement R-curve behavior without requiring the use of the crack growth direction. For R-curve behavior, this can be achieved by defining a spatially varying field, where the fracture parameters are set as a function of geometric coordinates. In the examples in this work, the fracture parameters could be made dependent on one coordinate (the x -coordinate for all specimens as shown in Figure 3 to Figure 5) though this would change depending on the configuration of the specimen and the pre-crack. This approach would be possible within Abaqus[®], where fracture parameters can be made dependent on a state variable, which can vary according to a given field. Separately, for tracking crack growth data at each node, this can be achieved by determining the minimum distance between a crack front node and any node defined as part of the initial crack front. This capability is currently not

implemented into either code, though could easily be done during post-processing or with a user subroutine.

More broadly, there are other differences between the implementation of the VCCT into Marc[™] and Abaqus[®]. Both codes implement the crack propagation modeling as a disconnection of a contact surface between two initially bonded or “glued” interfaces. However, while in Abaqus[®] this implementation is only available for use with a contact definition, in Marc[™] it is possible to apply this to multi-point constraints. Furthermore, in Marc[™], the VCCT can be used to model crack propagation by remeshing or by disconnecting elements along their edges, though at this stage these techniques are only available for 2D solid (plane stress/strain) or shells. Marc[™] also offers a user subroutine “ucrackgrow.f”, so that the crack growth behavior using the VCCT can be customized to specific requirements. This allows the user to control the crack growth direction, which is used to locate where the crack will propagate, and the amount of crack growth in an increment.

6.3 Solver comparison: Marc[™] and MD Nastran[™]

Comparing Marc[™], MD Nastran[™] SOL 400 and SOL 600, the results presented in this work indicate that the implementation of the VCCT is identical. However, as discussed previously, in general the range of technologies and options implemented into MD Nastran[™] tends to be limited, as it can take some time and several releases for aspects developed natively in Marc[™] to be migrated within the MD Nastran[™] environment [34]. As such, comparison of the codes is simplified to determining which of the technologies and options that are in Marc[™] are actually available within MD Nastran[™], and understanding what additional options need to be added to an MD Nastran[™] model to apply the VCCT technology. Critically, in this work MD Nastran[™] could not be used for any mixed-mode delamination growth specimens such as the SLB specimen as there were no mixed-mode criteria implemented. Additionally, SOL 400 and SOL 600 could not be applied with the SLB and ENF specimens due to the difficulties in using the default algorithm for determining the crack growth direction.

In terms of SOL 400, the VCCT implementation is integrated within the MD Nastran[™] nonlinear solver. In the analysis in this work, and in previous benchmark studies [47], the MD Nastran[™] nonlinear solver was more robust and efficient than in Marc[™]. This is partly due to a difference in the control of the increment size. In MD Nastran[™], this is based on the convergence parameters, while in Marc[™] control is framed around either the number of iterations in an increment or the damping parameter. Additionally, the SOL 400 solver in the version of MD Nastran[™] applied in this work (v2008.0) could not be used with user subroutines in order to customize the solver behavior. In Marc[™], the “ucrackgrow.f” subroutine can be used to define the crack growth direction and amount of crack growth, as previously discussed, and there are a wide range of other subroutines available to customize different aspects of the solver [23]. It was also seen that the SOL 400 had larger memory requirements, and generated larger output files and larger temporary files while running.

For SOL 600, as the solution runs natively in Marc[™], care needed to be taken with the MD Nastran[™] input deck to ensure that the model was translated into Marc[™] as intended. This required ensuring aspects such as the material orientations, element types and output requests were translated correctly, and that the cards controlling the VCCT technology were included. This was particularly challenging where aspects of one code did not easily “map” or translate into the other, or where access to Marc[™] functionality was limited by the keywords available in the MD Nastran[™] framework. To this end, an understanding of the Marc[™] input file and solver technologies was

considerably beneficial in ensuring that the MD Nastran™ input file was translated into a Marc™ input file with the appropriate format and content.

7. SUMMARY AND CONCLUSIONS

The delamination propagation simulation capabilities of the commercial FE codes Marc™ 2008r1 and MD Nastran™ v2008.0 with the VCCT were assessed. Benchmark delamination growth results for DCB, SLB and ENF specimens were generated using a previously developed numerical approach [26]. Experimental and analytical benchmark delamination growth results were taken from the literature for a second DCB specimen. Specimens were analyzed using 3D and 2D models, and compared to previous analyses using Abaqus® with the VCCT implemented. The results showed the following:

- The approach previously developed for using numerical benchmarks is a practical and efficient method for assessing delamination growth behavior. This approach offers advantages over benchmarking using experimental and analytical results for isolating code capabilities as it involves a direct comparison between identical models.
- The VCCT implementation in Marc™ and MD Nastran™ was capable of replicating the benchmark data for the DCB, ENF and SLB specimens, in terms of delamination growth behavior.
- For the Marc™ and MD Nastran® analyses, no issues were seen with convergence, so that no damping was applied, and in general, the analyses were not considered highly sensitive to the solver input parameters.
- The capacity in Marc™ and MD Nastran™ to automatically internally restart the increment after crack growth, and hence capture multiple crack growth events in one increment, was highly beneficial in terms of computational efficiency.
- Based on the previous two points, the analyses in Marc™ and MD Nastran™ were considerably more computationally efficient than those previously conducted in Abaqus®. Problems involving identical meshes across all codes took several hours in Marc™ and MD Nastran™, and several days in Abaqus®, although these were run on different machines.
- The implementation of VCCT in Marc™ and MD Nastran® uses a principal stress criterion to automatically determine the crack growth direction and hence explicitly locate the nodes required for crack propagation. This procedure was problematic for the problems considered and was not required in the Abaqus® analyses.
- For the SLB and ENF specimens, problems with the default automatic algorithm for determining crack growth direction in Marc™ and MD Nastran® were overcome by manually defining a suitable vector.
- The implementation of the VCCT in MD Nastran™ is a nominally identical, yet limited version of that available in Marc™, where the absence of mixed-mode crack growth and the option to specify a user-defined crack growth direction were critical in this work.
- The implementation of the VCCT in Marc™ and MD Nastran™ does not account for irregular mesh lengths ahead and behind the crack front.
- The use of mesh transition and fine mesh regions needed to be managed carefully in order to ensure an appropriate delamination front was formed.

Overall, it is clear that delamination propagation modeling is rapidly evolving in commercial FE codes, with each new software release introducing new technologies as well as refinements and extensions on previous technologies. This highlights the need for benchmarking techniques and examples that are capable of isolating and assessing the key requirements for delamination propagation simulation.

ACKNOWLEDGEMENTS

This material is based on work supported by National Aeronautics and Space Administration, Langley Research Center under Research Cooperative Agreement No. NNL09AA00A awarded to the National Institute of Aerospace. The research was supported by the Aircraft Aging and Durability Project as part of NASA's Aviation Safety Program. The analyses were performed at the Durability, Damage Tolerance and Reliability Branch at NASA Langley Research Center, Hampton, Virginia, USA. The authors would like to thank Per Nordlund of MSC.Software Corporation for his support and advice.

REFERENCES

- [1] T.K. O'Brien, Characterization of Delamination Onset and Growth in a Composite Laminate, in *Damage in Composite Materials*, ASTM STP 775: American Society for Testing and Materials, pp. 140-167, 1982.
- [2] A.C. Garg, Delamination - A Damage Mode in Composite Structures, *Engineering Fracture Mechanics*, vol. 29, pp. 557-584, 1988.
- [3] V.V. Bolotin, Delaminations in Composite Structures: Its Origin, Buckling, Growth and Stability, *Composites Part B: Engineering*, vol. 27B, pp. 129-145, 1996.
- [4] T.E. Tay, Characterization and Analysis of Delamination Fracture in Composites - An Overview of Developments from 1990 to 2001, *Applied Mechanics Reviews*, vol. 56, pp. 1-32, 2003.
- [5] R.H. Martin, Incorporating Interlaminar Fracture Mechanics into Design, in *International Conference on Designing Cost-Effective Composites: IMechE Conference Transactions*, London, U.K., pp. 83-92, 1998.
- [6] T.K. O'Brien, Fracture Mechanics of Composite Delamination, in *ASM Handbook, Volume 21, Composites*: ASM International, pp. 241-245, 2001.
- [7] ASTM D 5528-94a, Standard Test Method for Mode I Interlaminar Fracture Toughness of Unidirectional Fiber-Reinforced Polymer Matrix Composites, in *Annual Book of ASTM Standards*, vol. 15.03: American Society for Testing and Materials, 2000.
- [8] ASTM D 6671-01, Standard Test Method for Mixed Mode I-Mode II Interlaminar Fracture Toughness of Unidirectional Fiber Reinforced Polymer Matrix Composites, in *Annual Book of ASTM Standards*, vol. 15.03: American Society for Testing and Materials, 2000.
- [9] A.J. Russell and K.N. Street, Factors Affecting the Interlaminar Fracture Energy of Graphite/Epoxy Laminates, in *Progress in Science and Engineering of Composites*, T. Hayashi, K. Kawata, and S. Umekawa, Eds.: ICCM-IV, ASM International, Tokyo, pp. 279, 1982.
- [10] M. König, R. Krüger, K. Kussmaul, M. v. Alberti, and M. Gädke, Characterizing Static and Fatigue Interlaminar Fracture Behaviour of a First Generation Graphite/Epoxy Composite, in *Composite Materials: Testing and Design - (13th Vol.)*, ASTM STP 1242, S.J. Hooper, Ed.: American Society for Testing and Materials, pp. 60-81, 1997.
- [11] B.D. Davidson and W. Zhao, An Accurate Mixed-Mode Delamination Failure Criterion for Laminated Fibrous Composites Requiring Limited Experimental Input, submitted to, *Composites Science and Technology*, 2006.
- [12] T.K. O'Brien, Composite Interlaminar Shear Fracture Toughness, G_{IIc} : Shear Measurement or Shear Myth?, in *Composite Materials: Fatigue and Fracture, Seventh Volume*, ASTM STP 1330: American Society for Testing and Materials, pp. 3-18, 1998.
- [13] M.L. Benzeggagh and M. Kenane, Measurement of Mixed-Mode Delamination Fracture Toughness of Unidirectional Glass/Epoxy Composites with Mixed-Mode Bending Apparatus, *Composites Science and Technology*, vol. 56, pp. 439-449, 1996.
- [14] J. Reeder, 3D Mixed-Mode Delamination Fracture Criteria - An Experimentalist's Perspective, presented at American Society for Composites, 21st Annual Technical Conference, Dearborn, MI, USA, 2006.
- [15] S.M. Lee, An Edge Crack Torsion Method for Mode III Delamination Fracture Testing, *Journal of Composite Technology and Research*, pp. 193-201, 1993.
- [16] J.G. Ratcliffe, Characterization of the Edge Crack Torsion (ECT) Test for Mode III Fracture Toughness Measurement of Laminated Composites, National Aeronautics and Space Administration NASA/TM-2004-213269, 2004.
- [17] R.H. Martin, Evaluation of the Split Cantilever Beam for Mode III Delamination Testing, in *Composite Materials: Fatigue and Fracture (Third Volume)*, ASTM STP 1110: American Society for Testing and Materials, pp. 243-266, 1991.
- [18] P. Robinson and D.Q. Song, A New Mode III Delamination Test for Composites, *Advanced Composites Letters*, vol. 1, pp. 160-164, 1992.
- [19] E.F. Rybicki and M.F. Kanninen, A Finite Element Calculation of Stress Intensity Factors by a Modified Crack Closure Integral, *Engineering Fracture Mechanics*, vol. 9, pp. 931-938, 1977.
- [20] R. Krueger, Virtual Crack Closure Technique: History, Approach and Applications, *Applied Mechanics Reviews*, vol. 57, pp. 109-143, 2004.
- [21] Abaqus® 6.8 Documentation: Dassault Systèmes Simulia Corporation, Providence, RI, USA. 2008.
- [22] MD Nastran™ 2008 r1 Documentation: MSC.Software Corporation, Santa Ana, CA, USA. 2008.
- [23] Marc™ and Mentat™ 2008 r1 User Manuals: MSC.Software Corporation, Santa Ana, CA, USA. 2008.

- [24] M. Bruyneel, P. Morelle, and J.-P. Delsemme, Failure Analysis of Metallic and Composite Structures with SAMCEF, in NAFEMS Seminar: Materials Modeling – FE Simulations of the Behavior of Modern Industrial Materials Including their Failure, Niedernhausen, Germany. 2006.
- [25] D.M. Parks, The Virtual Crack Extension Method for Nonlinear Material Behavior, Computer Methods in Applied Mechanics and Engineering, vol. 12, pp. 353-364, 1977.
- [26] R. Krueger, An Approach to Assess Delamination Propagation Simulation Capabilities in Commercial Finite Element Codes, National Aeronautics and Space Administration NASA/TM-2008-215123, 2008.
- [27] G.A.O. Davies, Benchmarks for Composite Delamination, NAFEMS. East Kilbride, UK Report R0084, 2002.
- [28] R. Krüger, Three Dimensional Finite Element Analysis of Multidirectional Composite DCB, SLB and ENF Specimens, Institute for Statics and Dynamics of Aerospace Structures, University of Stuttgart ISD-Report No. 94/2, 1994.
- [29] B.D. Davidson, R. Krüger, and M. König, Effect of Stacking Sequence on Energy Release Rate Distributions in Multidirectional DCB and ENF specimens, Engineering Fracture Mechanics, vol. 55, pp. 557-569, 1996.
- [30] B.D. Davidson, R. Krüger, and M. König, Three Dimensional Analysis of Center Delaminated Unidirectional and Multidirectional Single Leg Bending Specimens, Composites Science and Technology, vol. 54, pp. 385-394, 1995.
- [31] R. Krueger and D. Goetze, Influence of Finite Element Software on Energy Release Rates Computed Using the Virtual Crack Closure Technique, National Institute of Aerospace NIA Report No. 2006-06, NASA/CR-214523, 2006.
- [32] A. Pieracci, B.D. Davidson, and V. Sundararaman, Nonlinear Analyses of Homogeneous, Symmetrically Delaminated Single Leg Bending Specimens, Journal of Composites Technology and Research, vol. 20, pp. 170-178, 1998.
- [33] KaleidaGraph User Manual: Synergy Software. 1996.
- [34] P. Nordlund, pers. comm. 2010.
- [35] B.D. Davidson, An Analytical Investigation of Delamination Front Curvature in Double Cantilever Beam Specimens, Journal of Composite Materials, vol. 24, pp. 1124-1137, 1990.
- [36] B.D. Davidson and R.A. Schapery, Effect of Finite Width on Deflection and Energy Release Rate of an Orthotropic Double Cantilever Specimen, Journal of Composite Materials, vol. 22, pp. 640-656, 1988.
- [37] M. König, R. Krüger, and S. Rinderknecht, Finite Element Analysis of Delamination Growth in a Multidirectional Composite ENF Specimen, in Composite Materials: Theory and Practice, ASTM STP 1383, P. Grant and C.Q. Rousseau, Eds.: American Society for Testing and Materials, pp. 345-365, 2000.
- [38] R. Krüger, M. König, and T. Schneider, Computation of Local Energy Release Rates Along Straight and Curved Delamination Fronts of Unidirectionally Laminated DCB- and ENF - Specimens, in Proceedings of the 34th AIAA/ASME/ASCE/AHS/ASC SSDM Conference, La Jolla, CA: American Institute of Aeronautics and Astronautics, Washington, pp. 1332-1342, 1993.
- [39] I.S. Raju, K.N. Shivakumar, and J.H. Crews, Three-Dimensional Elastic Analysis of a Composite Double Cantilever Beam Specimen, AIAA Journal, vol. 26, pp. 1493-1498, 1988.
- [40] L.A. Carlsson, J.W. Gillespie, and R.B. Pipes, On the Analysis and Design of the End Notched Flexure (ENF) Specimen for Mode II Testing, Journal of Composite Materials, vol. 20, pp. 594-604, 1986.
- [41] P. Davies, B.R.K. Blackman, and A.J. Brunner, Standard Test Method for Delamination Resistance of Composite Materials: Current Status, Applied Composite Materials, vol. 5, pp. 345-364, 1998.
- [42] T.K. O'Brien, G.B. Murri, and S.A. Salpaekar, Interlaminar Shear Fracture Toughness and Fatigue Thresholds for Composite Materials, in Composite Materials: Fatigue and Fracture, Second Volume ASTM STP 1012, P.A. Lagace, Ed.: American Society for Testing and Materials, pp. 222-250., 1989.
- [43] A.C. Orifici, R.S. Thomson, R. Degenhardt, C. Bisagni, and J. Bayandor, Development of a Finite-Element Methodology for the Propagation of Delaminations in Composite Structures, Mechanics of Composite Materials, vol. 43, pp. 9-28, 2007.
- [44] A.C. Orifici, R.S. Thomson, R. Degenhardt, S. Büsing, and J. Bayandor, Development of a Finite Element Methodology for Modelling Mixed-Mode Delamination Growth in Composite Structures, in 12th Australian International Aerospace Congress, Melbourne, Australia. 2007.
- [45] R. Krueger, Assessment of Delamination Propagation Capabilities in Commercial Finite Element Codes, in ASC 23rd Technical Conference on Composite Materials, Memphis, TN, USA. 2008.
- [46] P. Robinson and D.Q. Song, A Modified DCB Specimen for Mode I Testing of Multidirectional Laminates, Journal of Composite Materials, vol. 26, pp. 1554-1577, 1992.

- [47] A.C. Orifici, R.S. Thomson, A.J. Gunnion, R. Degenhardt, H. Abramovich, and J. Bayandor, Benchmark Finite Element Simulations of Postbuckling Composite Stiffened Panels, in 11th Australian International Aerospace Congress, Melbourne, Australia. 2005.

TABLE 1. MATERIAL PROPERTIES.

T300/1076 Unidirectional Graphite/Epoxy Prepreg		
$E_{11} = 139.4$ GPa	$E_{22} = 10.16$ GPa	$E_{33} = 10.16$ GPa
$\nu_{12} = 0.30$	$\nu_{13} = 0.30$	$\nu_{23} = 0.436$
$G_{12} = 4.6$ GPa	$G_{13} = 4.6$ GPa	$G_{23} = 3.54$ GPa
C12K/R6376 Unidirectional Graphite/Epoxy Prepreg		
$E_{11} = 146.9$ GPa	$E_{22} = 10.6$ GPa	$E_{33} = 10.6$ GPa
$\nu_{12} = 0.33$	$\nu_{13} = 0.33$	$\nu_{23} = 0.33$
$G_{12} = 5.45$ GPa	$G_{13} = 5.45$ GPa	$G_{23} = 3.99$ GPa
T800/924 Unidirectional Graphite/Epoxy Prepreg		
$E_{11} = 126$ GPa	$E_{22} = 7.5$ GPa	$E_{33} = 7.5$ GPa
$\nu_{12} = 0.263$	$\nu_{13} = 0.263$	$\nu_{23} = 0.263$
$G_{12} = 4.981$ GPa	$G_{13} = 4.981$ GPa	$G_{23} = 3.321$ GPa
	$G_{Ic} = 0.281$ kJ/m ²	

The material properties are given with reference to the ply coordinate axes where index 11 denotes the ply principal axis that coincides with the direction of maximum in-plane Young’s modulus (fiber direction). Index 22 denotes the direction transverse to the fiber in the plane of the lamina and index 33 denotes the direction perpendicular to the plane of the lamina.

TABLE 2. FINITE ELEMENT MODELS.

Model	FE Solver	Dimension	Reference	Benchmark
DCB-1	Marc TM	2D	Figure 7a	Numerical – Marc TM
		3D	Figure 7b	
	MD Nastran TM SOL 400	2D	Figure 7a	
		3D	Figure 7b	
	MD Nastran TM SOL 600	2D	Figure 7a	
		3D	Figure 7b	
	Abaqus [®]	3D	Figure 7b [26]	Numerical – Abaqus [®]
DCB-2	Marc TM	2D	Figure 7a	Experimental [46] and analytical [27]
		3D	Figure 7b *	
	Abaqus [®]	2D	Figure 7a [45]	
		3D	Figure 7b [45]	
SLB	Marc TM	3D	Figure 8	Numerical – Marc TM
ENF	Marc TM	2D	Figure 9a	Numerical – Marc TM
		3D	Figure 9b	
ENF refined mesh	Marc TM	3D	Figure 10	Numerical – Marc TM

* Width increased from model shown, from 25 mm to 30 mm, by duplicating elements, so that the mesh length in the width direction remained unchanged.

APPENDIX

Example input for VCCT analysis in Marc™ and MD Nastran™

The input required to perform VCCT analysis in Marc™, MD Nastran™ SOL 400 and SOL 600 is discussed in the following paragraphs. This is focused exclusively on the keywords and parameters of relevance for VCCT analysis, where for further detail reference should be made to the software documentation [23, 22]. Note that the ellipses “...” are used to indicate removed text. Also, in most cases example values are included as taken from an input file, and these should not be implied as fixed, recommended or necessary unless otherwise stated.

Example input for Marc™

The key parameters required for VCCT analysis in Marc™ are listed below. Note that in this work input files were completely generated using the Mentat™ pre-processor.

Model definition options

Crack front node set: This is useful for the VCCT card.

```
define                ndsq                set    crack1_nodes
      8572             8580                8588    8596        8644
...
...
```

Contact body: The properties that control the contact and the two bounding bodies (groups of elements) that form the crack interface.

```
contact
2, 0      ...
...
$....contact body 1: cbody_top
...
$....contact body 2: cbody_bot
...
```

VCCT parameters: Parameters that control the VCCT implementation.

```
vcct
      1
      1      2
crack1
crack1_nodes
  2, <a>, 0, <b>
0.0, 0.0, <GIc>, <GIIC>, <GIIIc>, <n1>, 0.0, 0.0, ...
...
<d1>,<d2>,<d3>
```

where <a> is the code for crack growth direction method (1 for principal stress criterion, 4 for a specified vector), is the code for crack growth criterion (2 for single-mode, 4 for Reeder), <GIC>, <GIIC>, <GIIIC> are the fracture toughness values, <n1> is the Reeder exponent used if =4, and <d1>, <d2>, <d3> are the x, y, z components of the crack growth direction if <a>=4.

Note that it is not required to tell the code which contact interfaces are associated with the crack. The user only inputs the crack front nodes, and the solver will determine which contact interface these nodes are associated with.

History definition options

Multiple load cases: Useful to perform a multiple-step analysis to save computation time when the initiation point for crack growth is approximately known (use the standard `loadcase` card).

Nodal output: Useful output to plot in order to visualize the crack front data, where the crack front images in this report were generated primarily using the “glue deactivation status”.

```

post
...
nodal, 38      → contact status
nodal, 58      → GI
nodal, 59      → GII
nodal, 60      → GIII
nodal, 73      → glue deactivation status
nodal, 74      → VCCT failure index

```

Example input for MD Nastran™ SOL 400 and SOL 600

Examples of the parameters required for conducting VCCT analysis in MD Nastran™ SOL 400 and SOL 600 are given below, which follow the comments given previously. In this work, the input decks were generated using MSC Patran™, with minor editing in order to add parameters necessary for VCCT. These are specified below, which also includes other parameters of relevance to VCCT. In general, the input files for SOL 400 and SOL 600 are mostly identical, except for a few keywords. The comments to the right of the page indicate which parameters are exclusive for each solver, and where these are absent the parameters relate to both solvers.

Executive control statement

```

SOL 400      → SOL 400 only

SOL 600,NLSTATIC OUTR=xdb      → SOL 600 only

```

Case control

VCCT = 1

→ reference to bulk data entry

Multiple load cases: Useful to perform a multiple-step analysis to save computation time when the initiation point for crack growth is approximately known (use the standard SUBCASE card).

```
SUBCASE 1
STEP 1           → SOL 400 only
  ANALYSIS = NLSTATIC → SOL 400 only
  ...

SUBCASE 2
STEP 2           → SOL 400 only
  ANALYSIS = NLSTATIC → SOL 400 only
  ...

BEGIN BULK
```

Contact body: The parameters relating to the glued contact definition.

```
BCPARA  0          NLGLUE  1          NBODIES  2          ...

BCTABLE  0
  SLAVE   2          0.          0.          0.          0.          1
          2          0          0
          FBSH  1.+20  .9          0.
  MASTERS 1

BCTABLE  1
  SLAVE   2          0.          0.          0.          0.          1
          2          0          0
          FBSH  1.+20  .9          0.
  MASTERS 1
```

VCCT parameters: Parameters that control the VCCT implementation.

```
VCCT, 1, 1, 2
, <GIc>, , , , , <GIIC>, <GIIIc>
...
<nodes>
```

where <G1c>, <GIIc>, <GIIIc> are the fracture toughness values, and <nodes> is either a sequence of node numbers or the negative index of a node set (to avoid confusion with node numbers).

Crack front node set. Example of a node set, here assigned number “9”, which would be referenced as “-9” in the VCCT statement above.

```
SET3          9   GRID   8572   8580   8588   ...
...

```

Nonlinear solution parameters: In SOL 400 and SOL 600, the NLPARM card is used. In this work, in addition to the NLPARM card, for SOL 400 the NLADAPT card was used, and for SOL 600 the NLAUTO and NLSTRAT cards were used. This was done in order to ensure that the nonlinear solution scheme was consistent between solvers as much as possible.

Element properties: In SOL 400 only, an additional element property card is required to access advanced properties required for VCCT. Examples are given below for 3D solid elements (which reference the PSOLID card) and 2D plane strain elements (which reference the PLPLANE card).

```
PSOLID        1      1      1      REDUCED
PSLDN1        1      1
              C8   SOLID      L

PLPLANE       1      1
PSHLN2        1      1      1      25.
              C4   PLSTRN     L

```

Contact body: The two bounding bodies (groups of elements) that form the crack interface (here an example for 3D, for 2D replace “2D” with “3D” in the third parameter of BCBODY).

```
$ Deform Body Contact LBC set: cbody_top
BCBODY  1      3D      DEFORM  1      0
BSURF   1      385     386     387     ...
...
$ Deform Body Contact LBC set: cbody_btm
BCBODY  2      3D      DEFORM  2      0
BSURF   2      385     386     387     ...
...

```

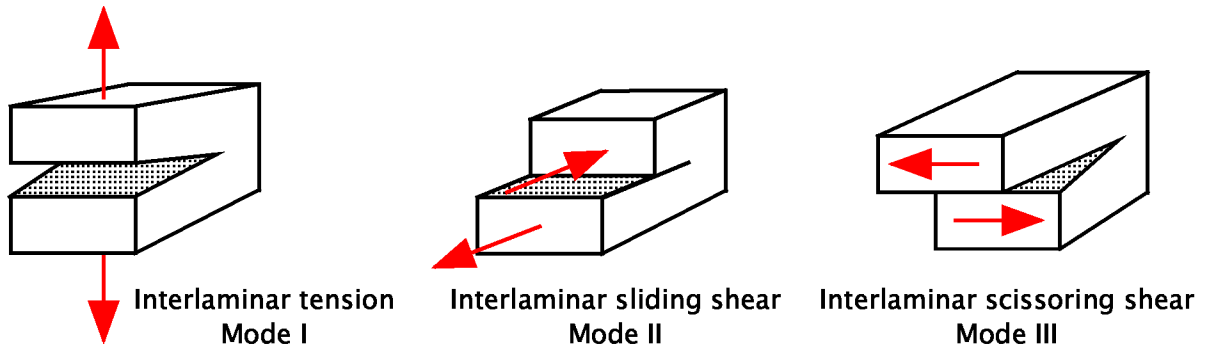


Figure 1. *Fracture modes.*

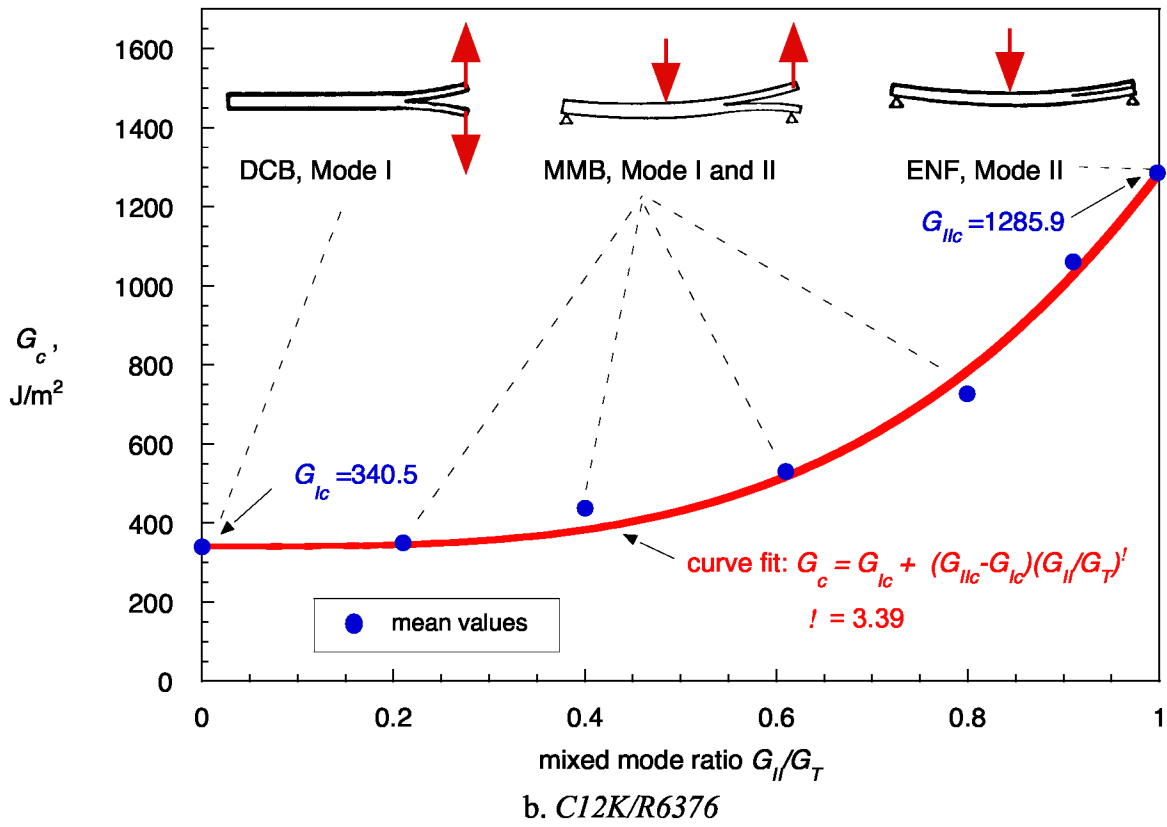
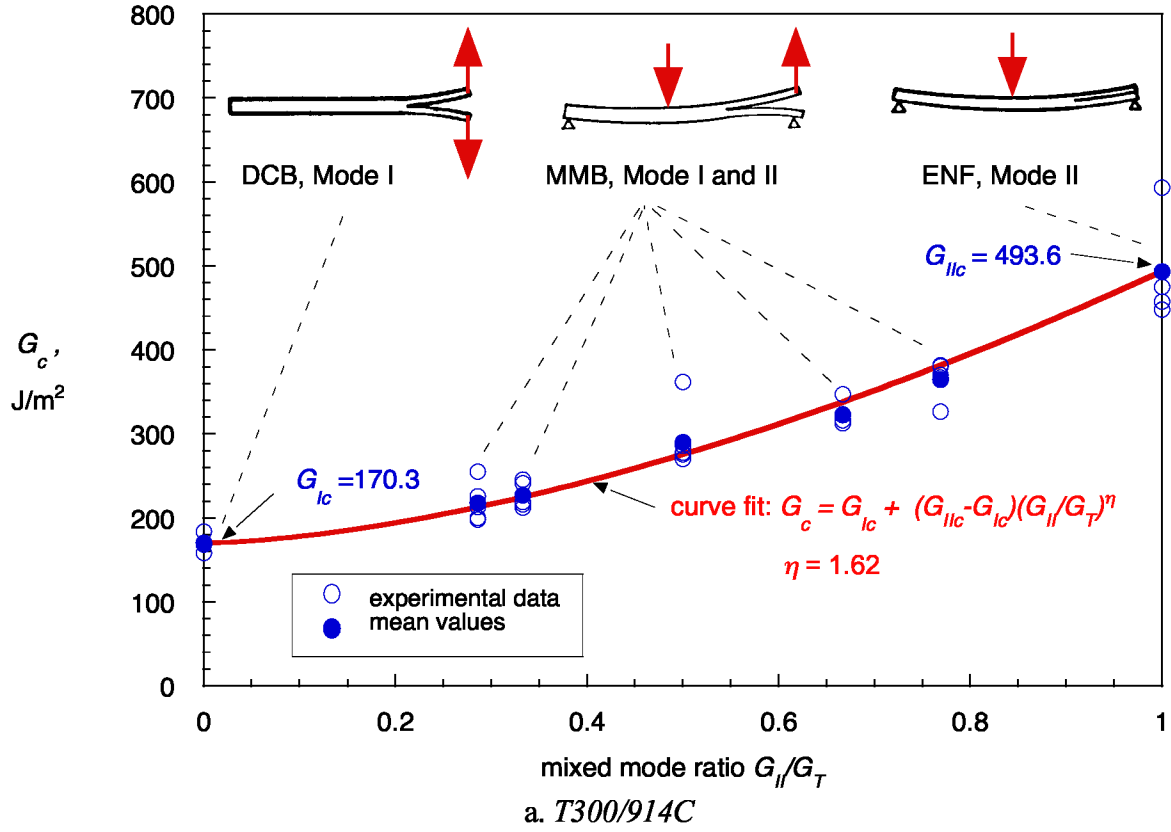
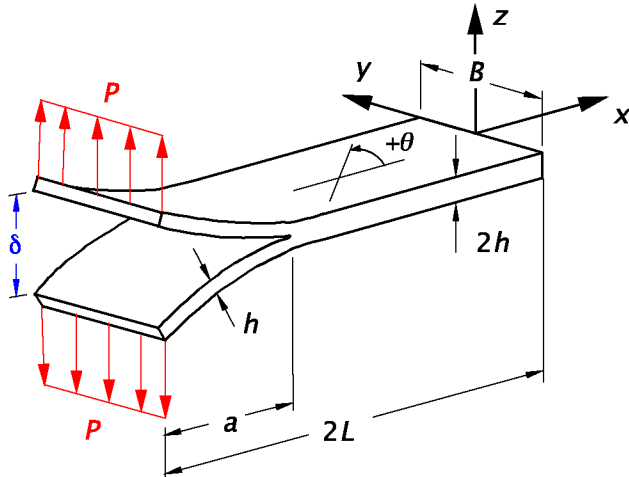
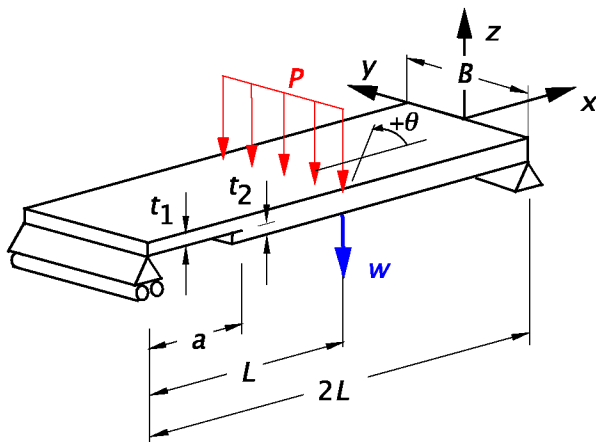


Figure 2. Mixed-mode fracture criterion for composite materials.



	DCB-1	DCB-2
B	25.0 mm	30.0 mm
$2h$	3.0 mm	3.0 mm
$2L$	150.0 mm	150.0 mm
a	30.0 mm	30.0 mm
	T300/1076	T800/924
	unidirectional	unidirectional

Figure 3. DCB-1 and DCB-2 specimens.

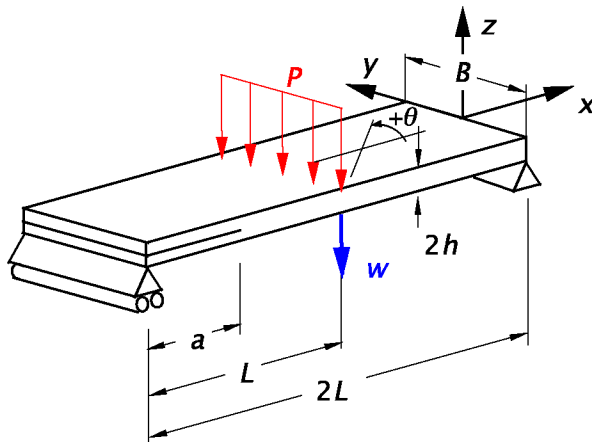


B	25.4 mm
t_1	2.032 mm
t_2	2.032 mm
$2L$	177.8 mm
a	34.29 mm

C12K/R6376

$[\pm 30/0/-30/0/30/0_4/30/0/-30/0/-30/30 // -30/30/0/30/0/-30/0_4/-30/0/30/0/\pm 30]$

Figure 4. SLB specimen.



B	25.0 mm
$2h$	3.0 mm
L	70.0 mm
$2L$	140.0 mm
a	30.0 mm

T300/1076
unidirectional

Figure 5. ENF specimen.

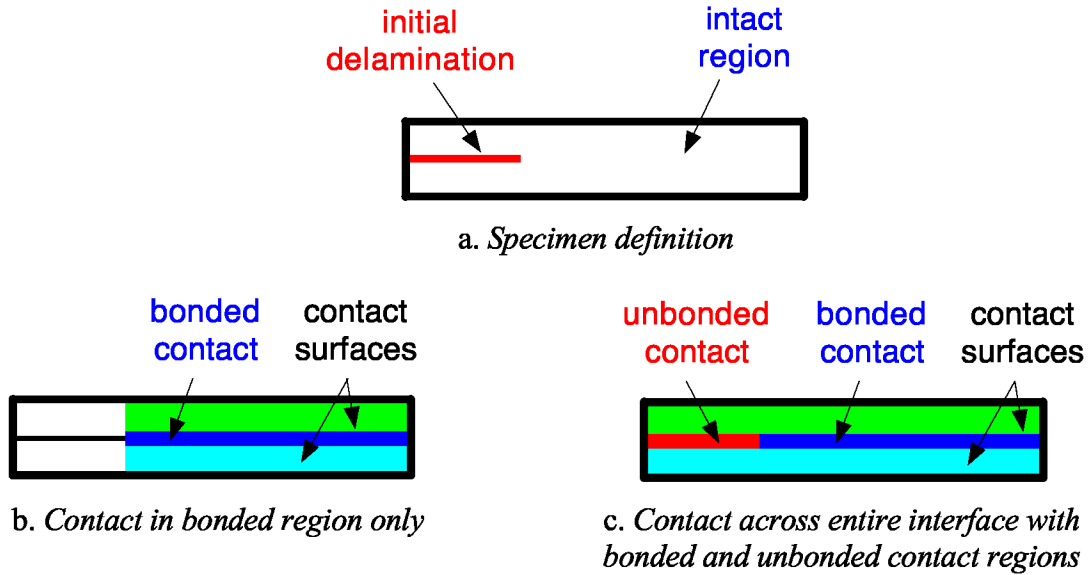


Figure 6. Contact-based crack modeling.

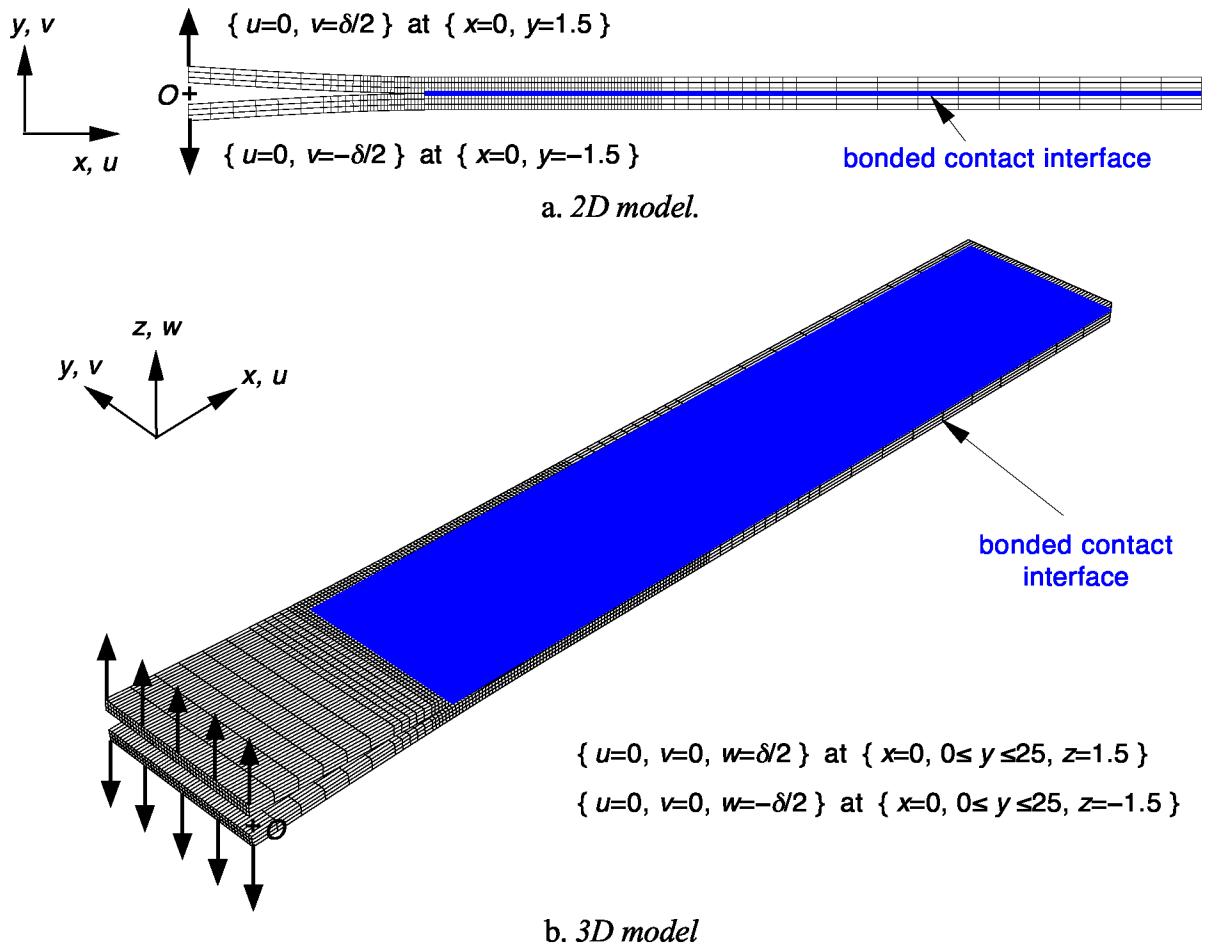


Figure 7. DCB-I deformed specimen mesh with boundary conditions.

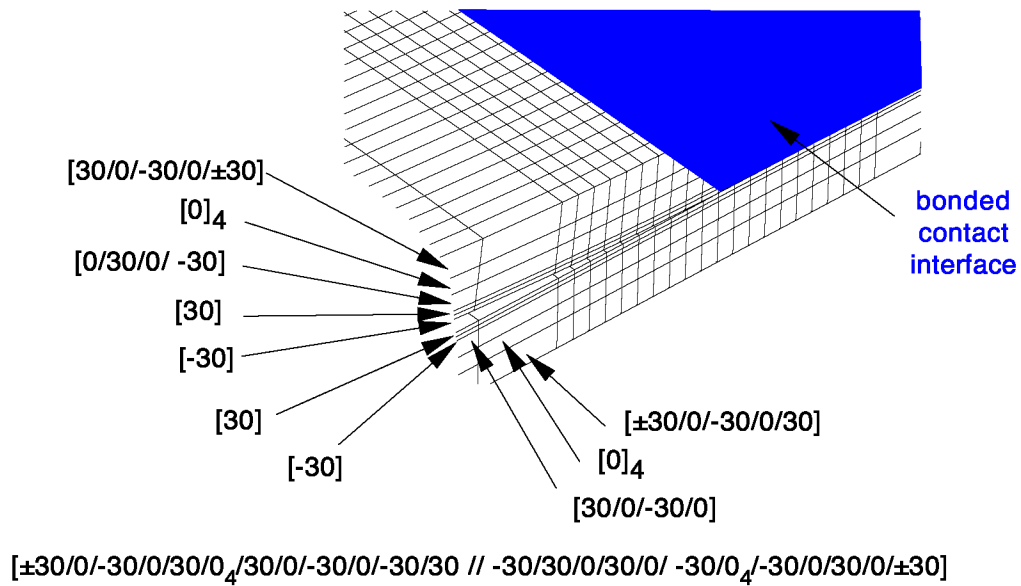
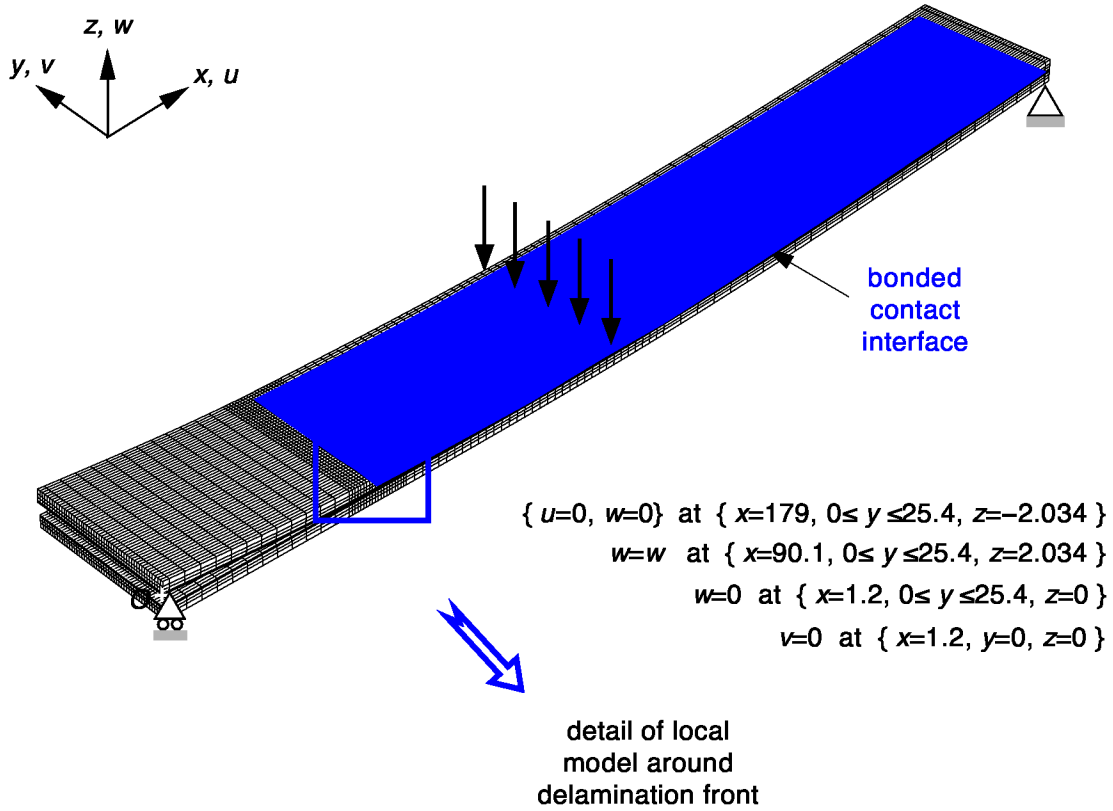


Figure 8. Deformed mesh of SLB specimen and detail of region around delamination front with boundary conditions.

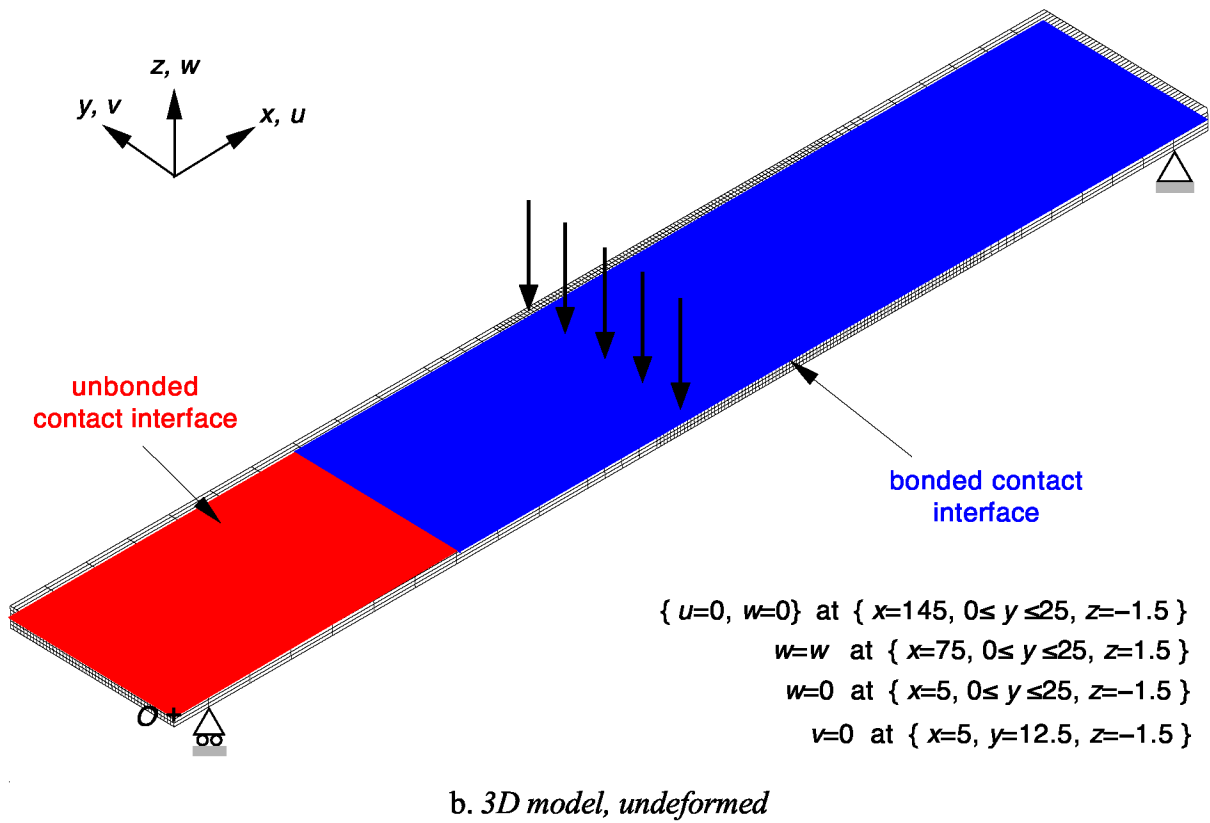
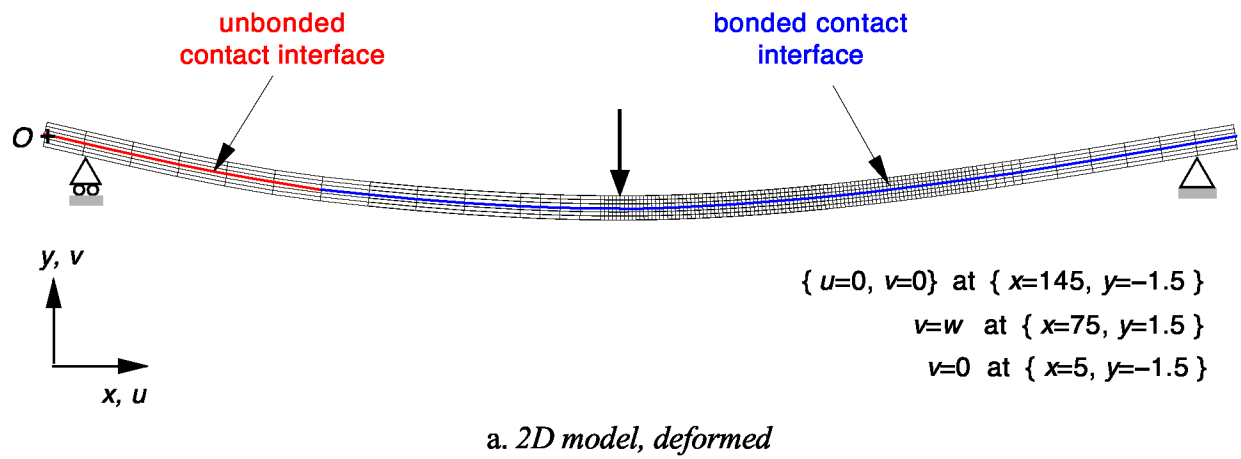


Figure 9. ENF specimen mesh with boundary conditions.

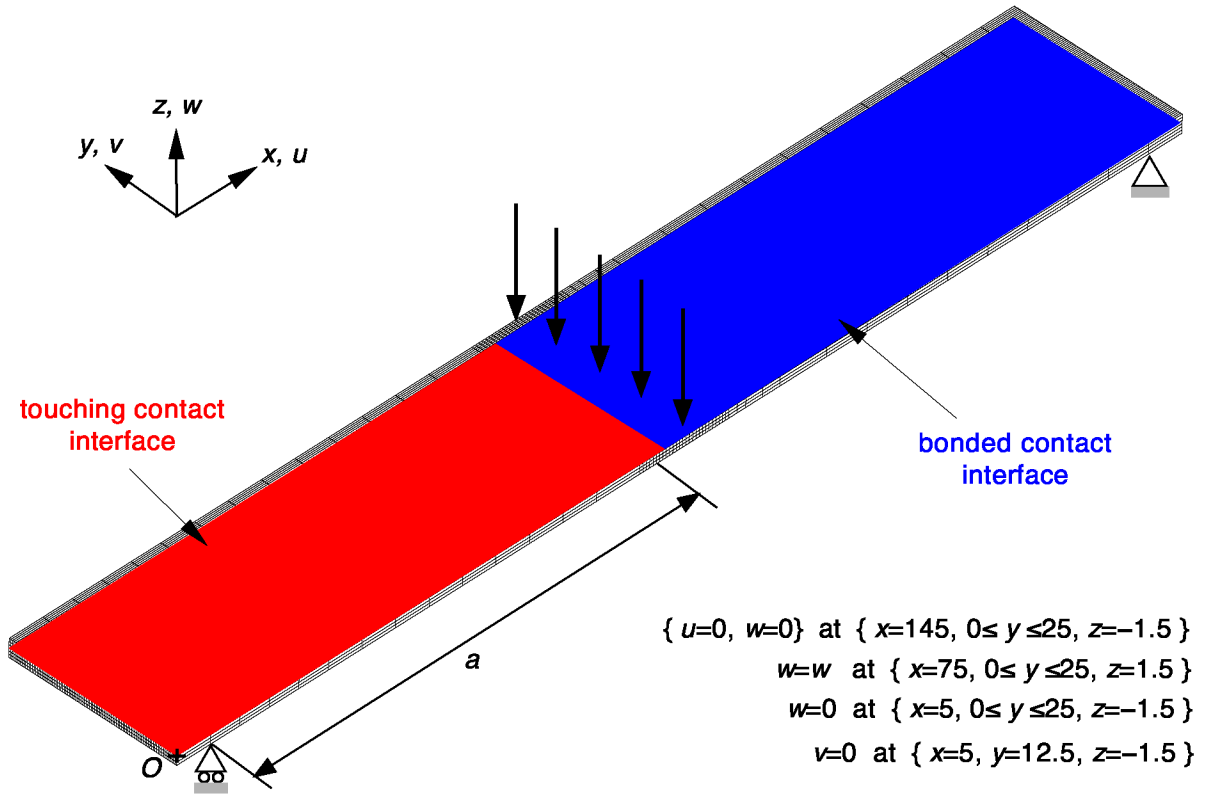


Figure 10. ENF refined mesh ($a = 65 \text{ mm}$).

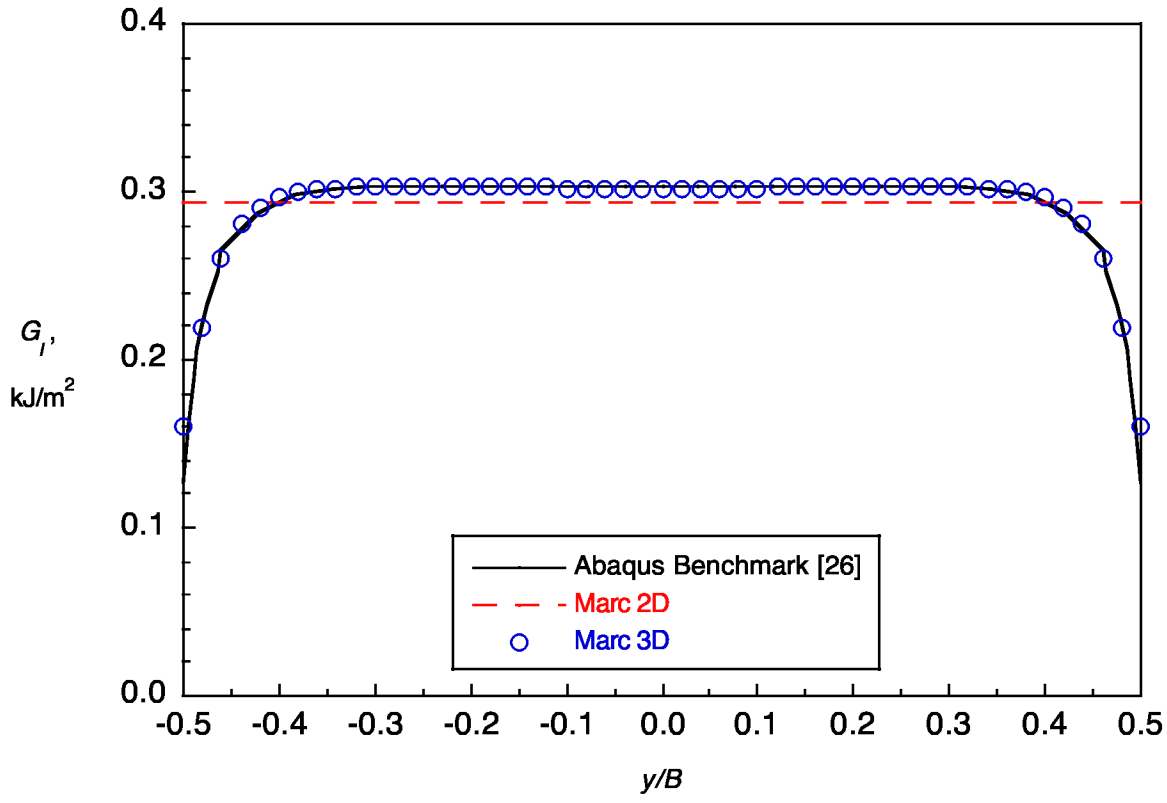


Figure 11. Strain energy release rate distribution, DCB ($a = 30.5 \text{ mm}$, $\delta/2 = 1.0 \text{ mm}$).

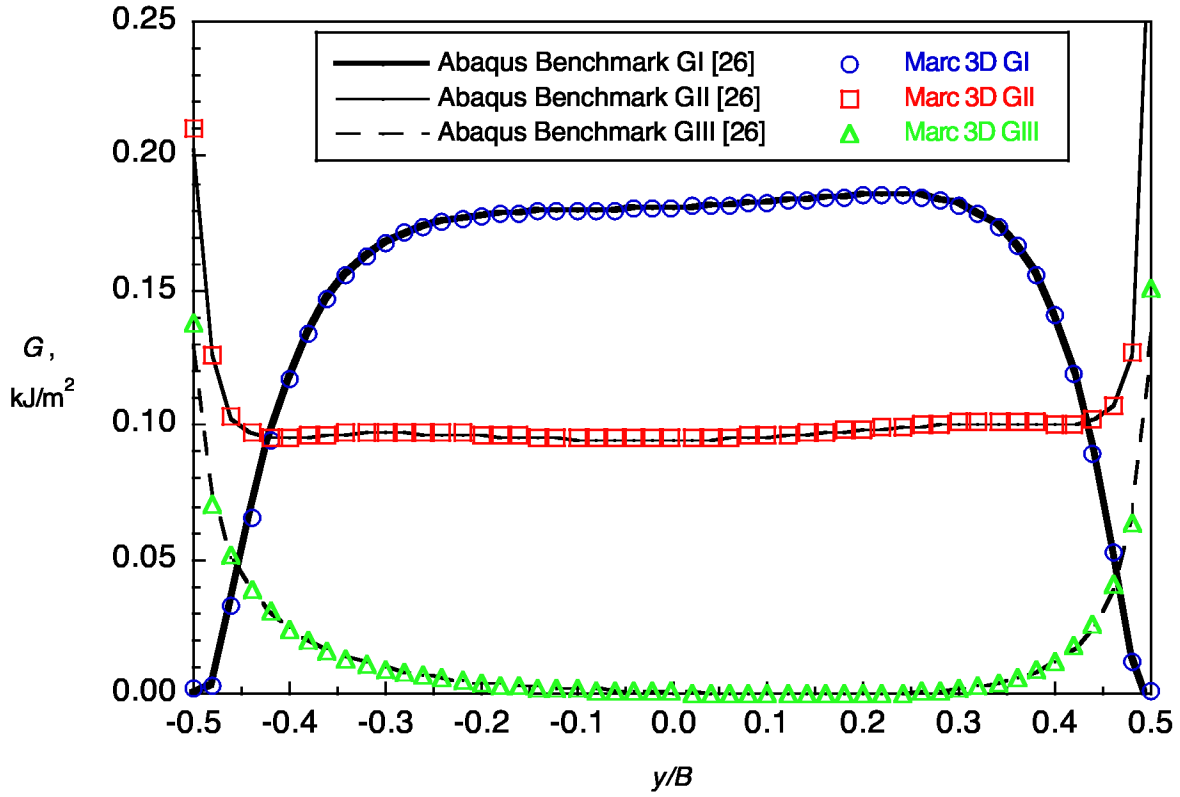


Figure 12. Strain energy release rate distribution, SLB ($a = 31 \text{ mm}$, $w = 2.8 \text{ mm}$).

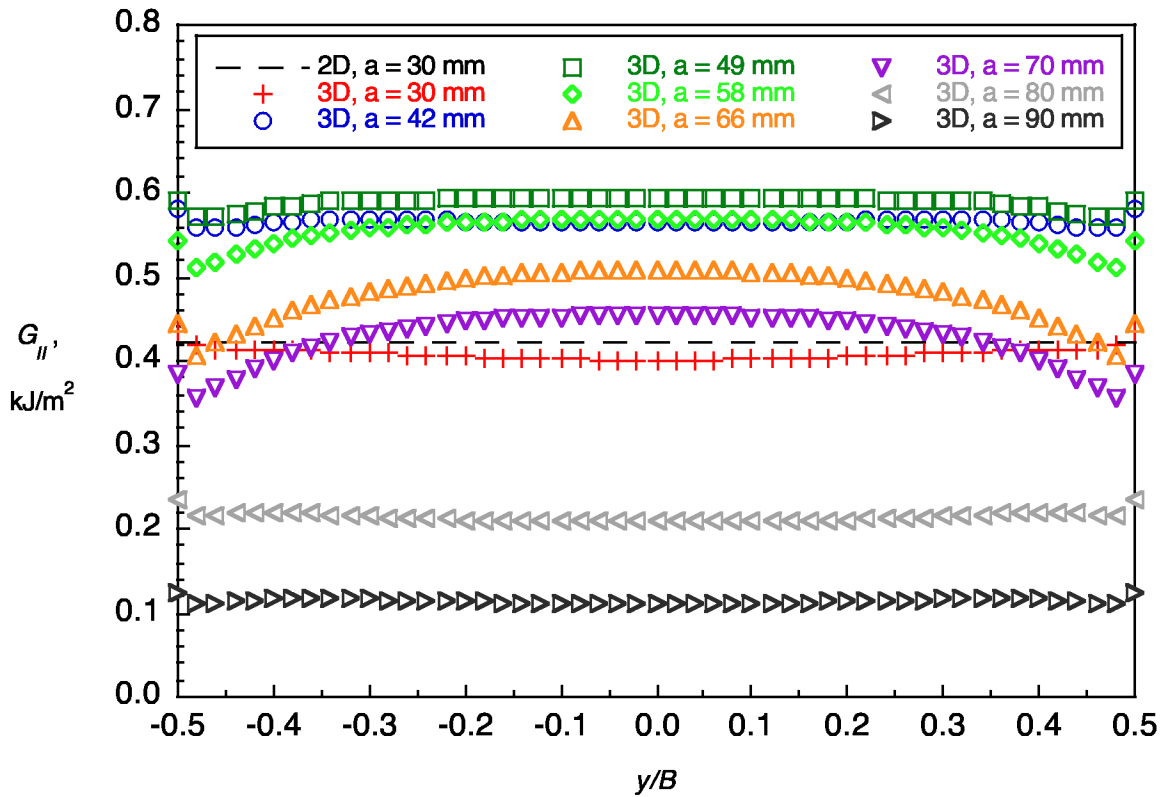


Figure 13. Strain energy release rate distribution, ENF ($w = 4.0 \text{ mm}$).

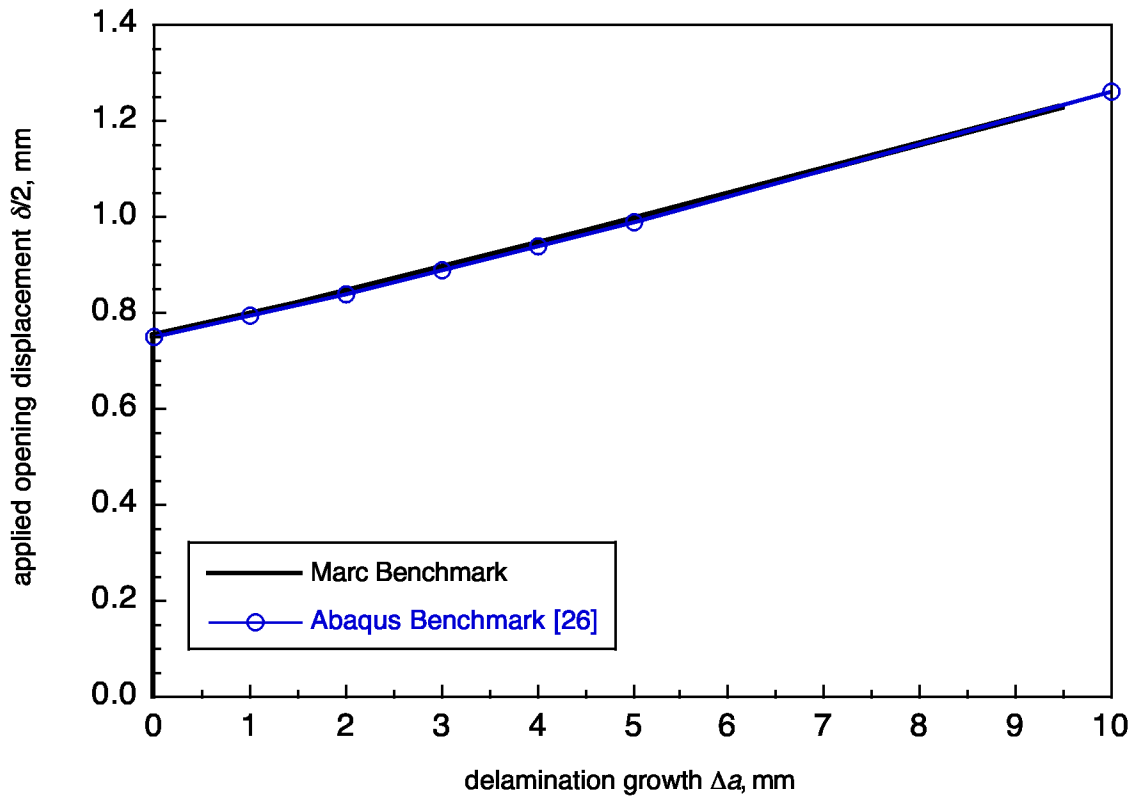


Figure 14. *DCB-1*, benchmark delamination growth results.

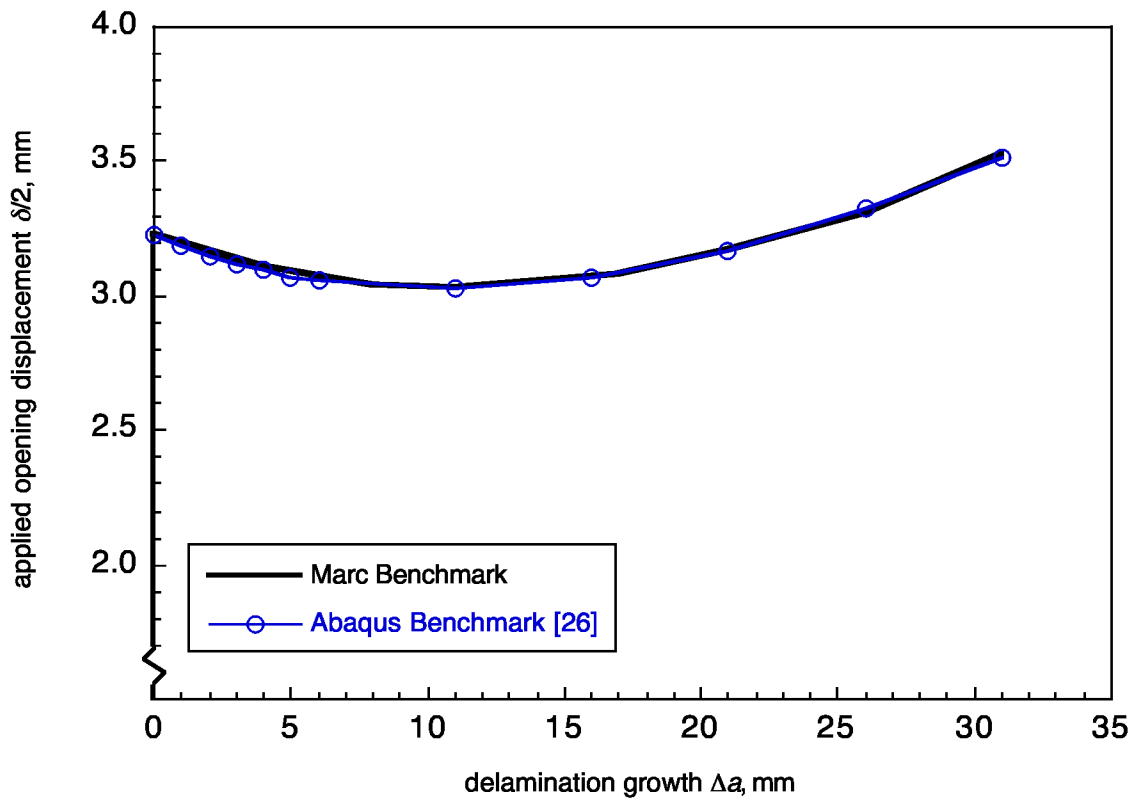


Figure 15. *SLB*, benchmark delamination growth results.

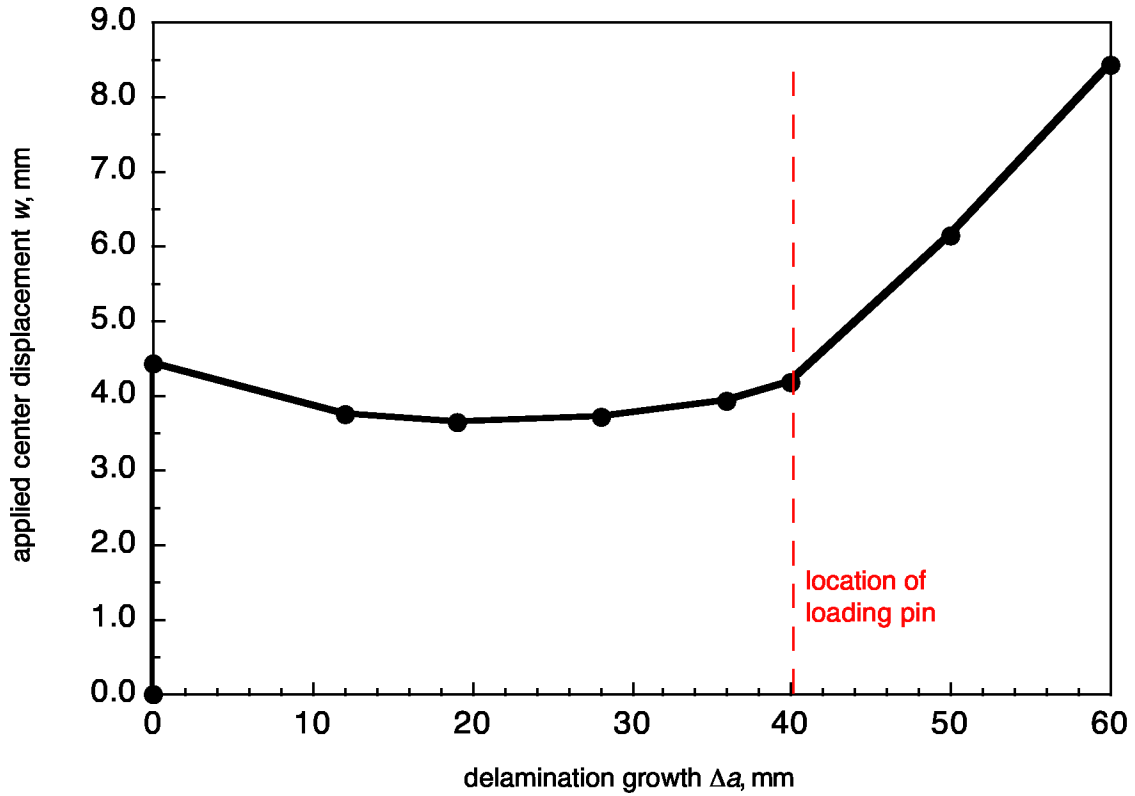


Figure 16. ENF, Marc benchmark delamination growth results.

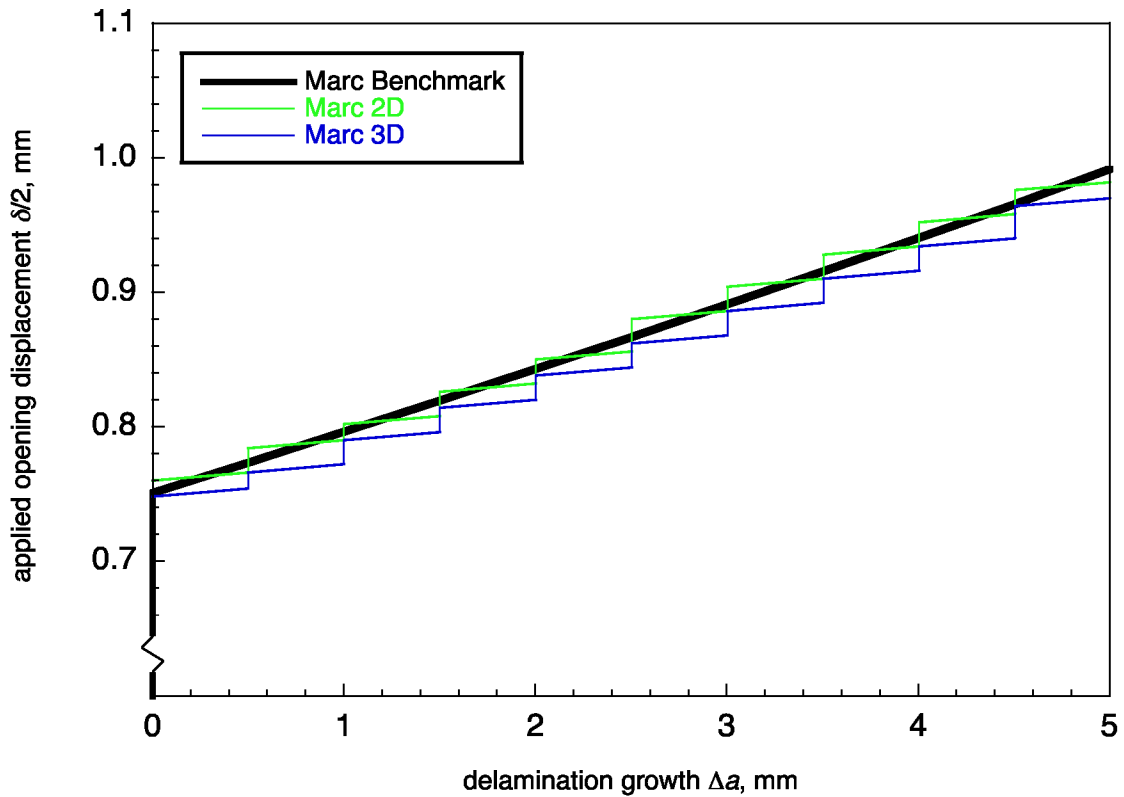


Figure 17. DCB-I, applied displacement versus delamination growth.

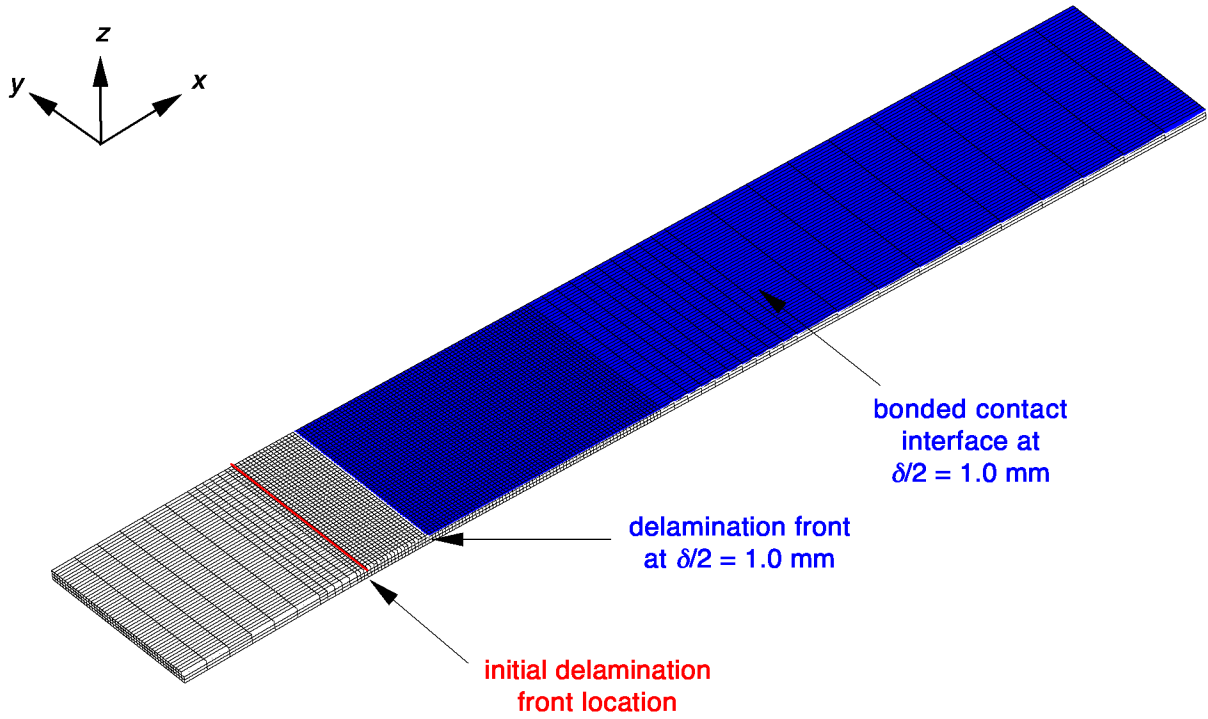


Figure 18. DCB-I bottom sublaminates deformed mesh at $\delta/2 = 1.0$ mm, with delamination interface.

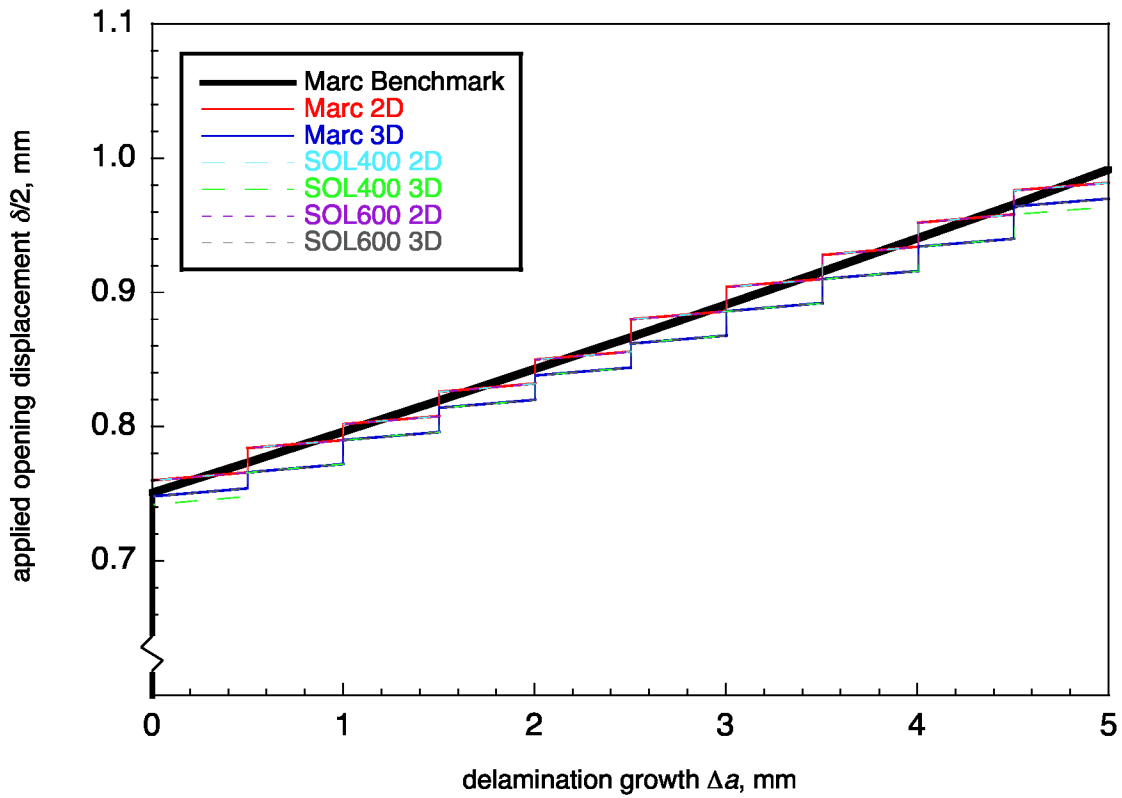


Figure 19. DCB-I, applied displacement versus delamination growth.

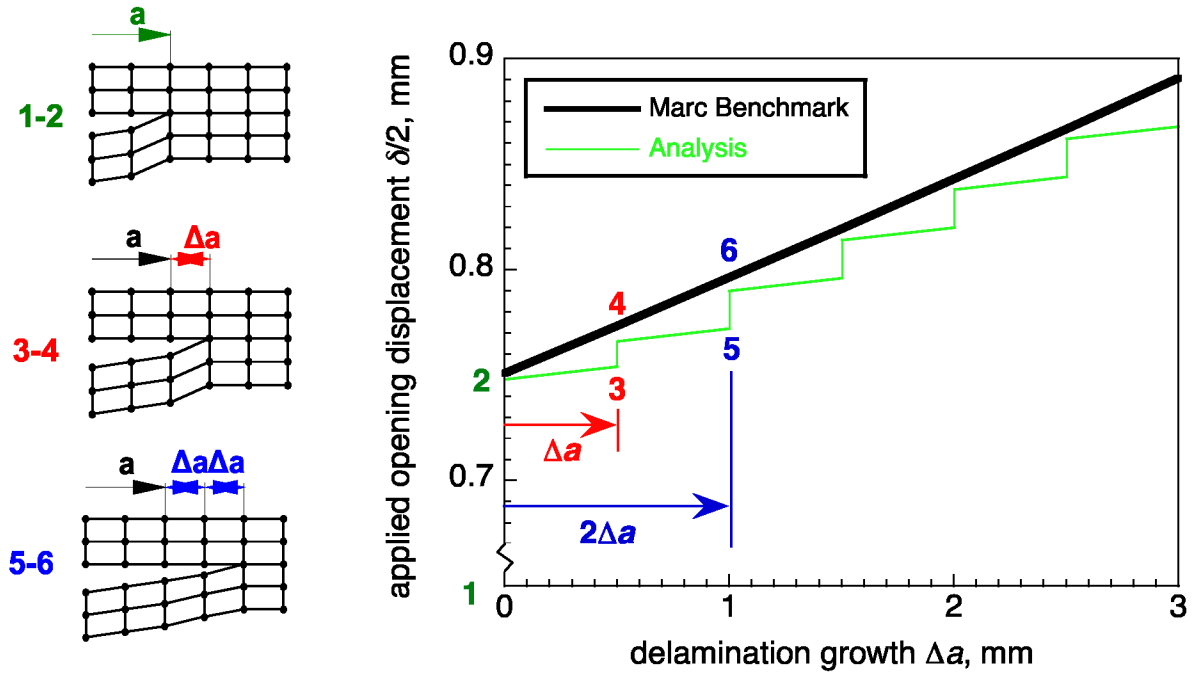


Figure 20. Delamination growth behavior.

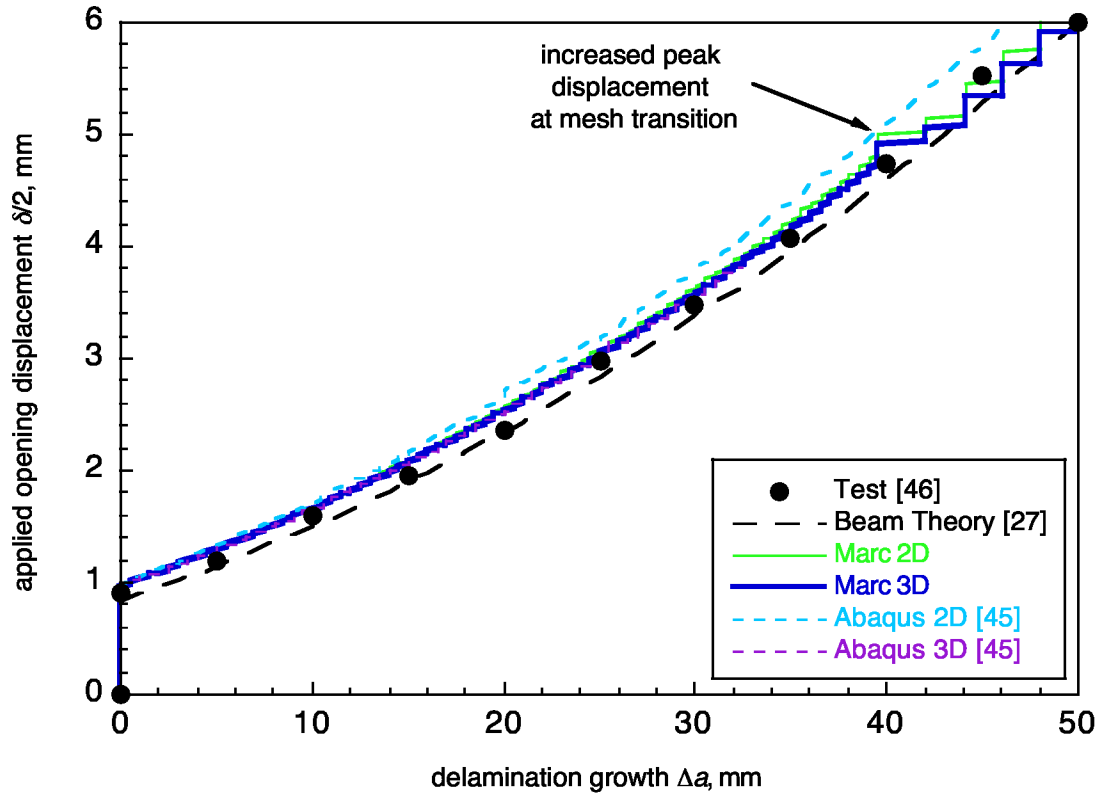


Figure 21. DCB-2, applied displacement versus delamination growth.

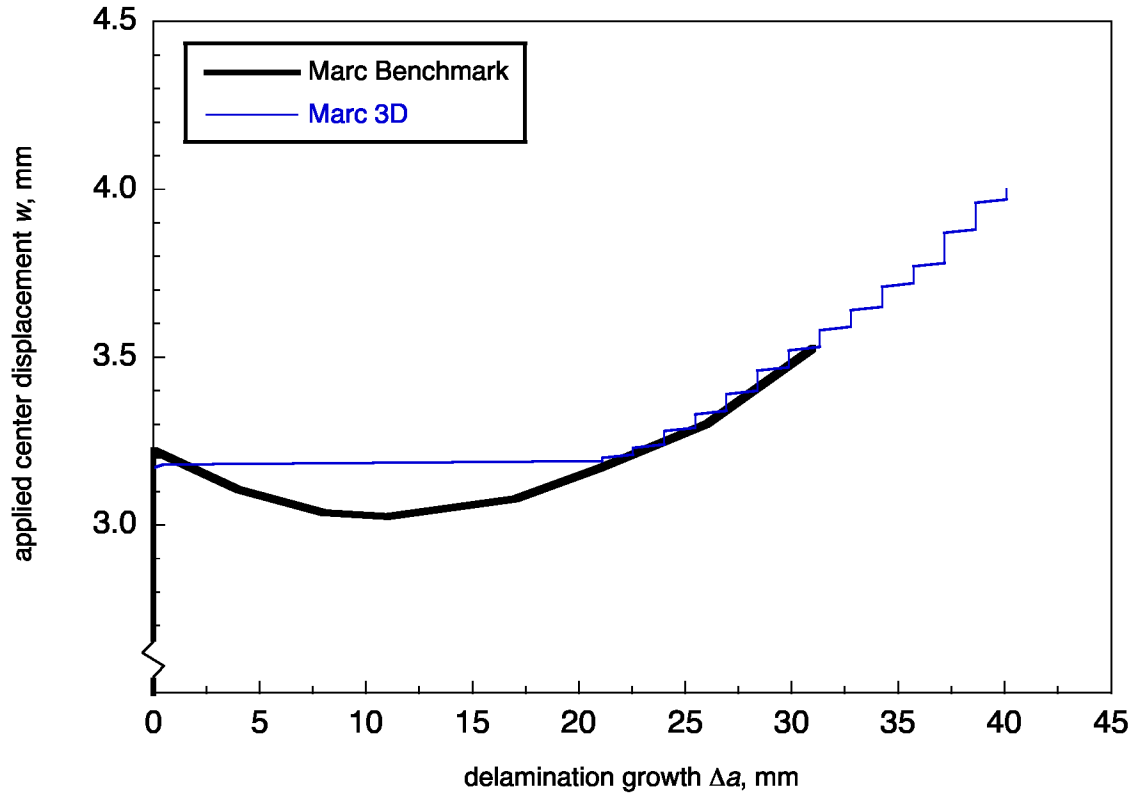


Figure 22. SLB, applied displacement versus delamination growth.

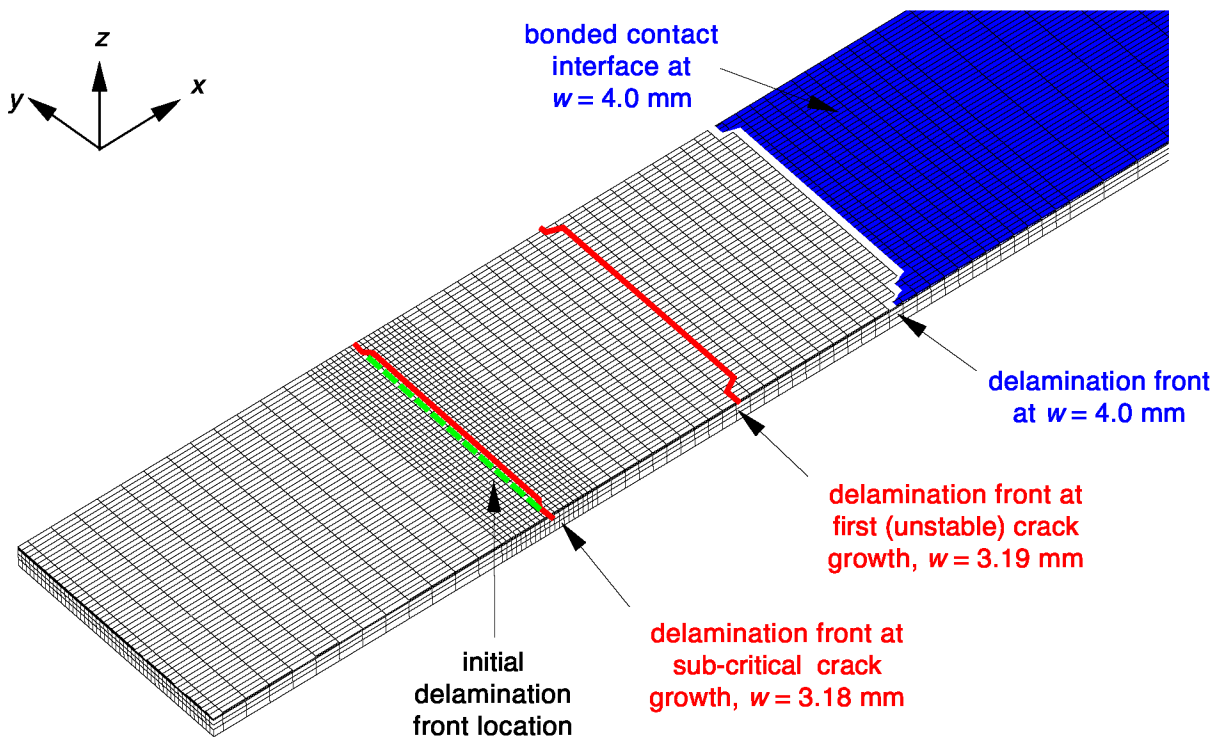


Figure 23. SLB bottom sublaminates mesh with delamination front progression.

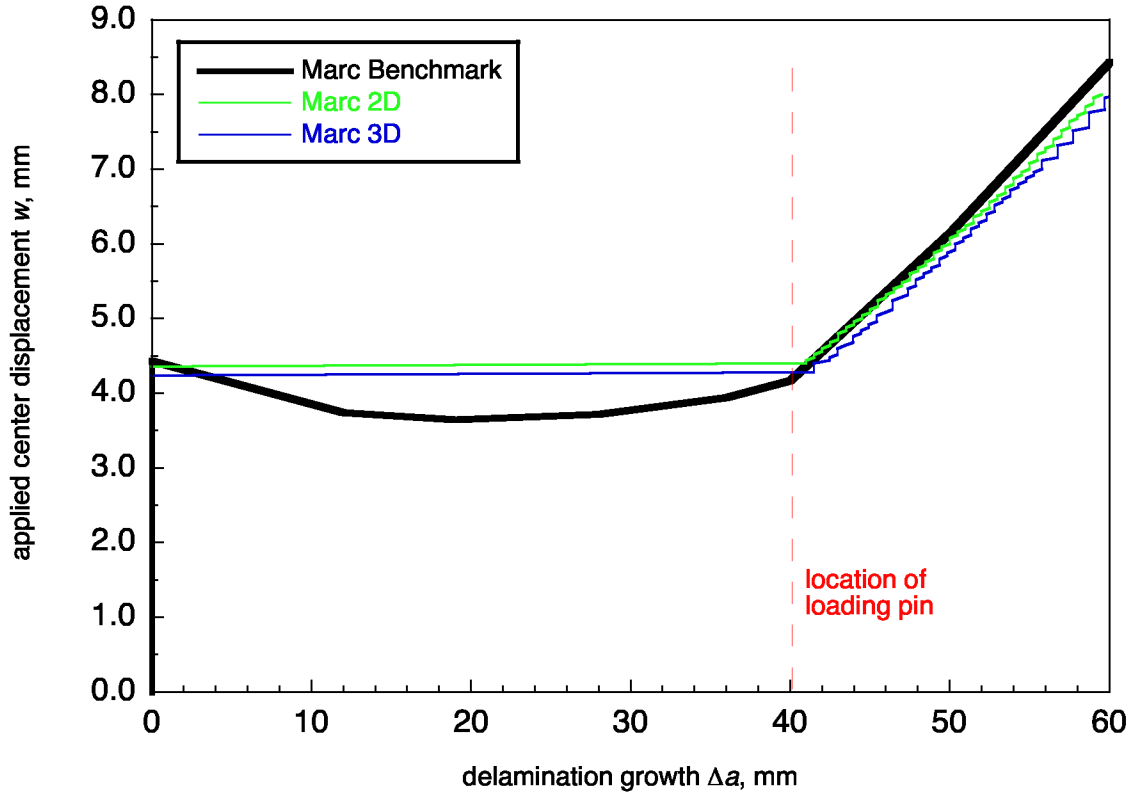


Figure 24. ENF, applied displacement versus delamination growth.

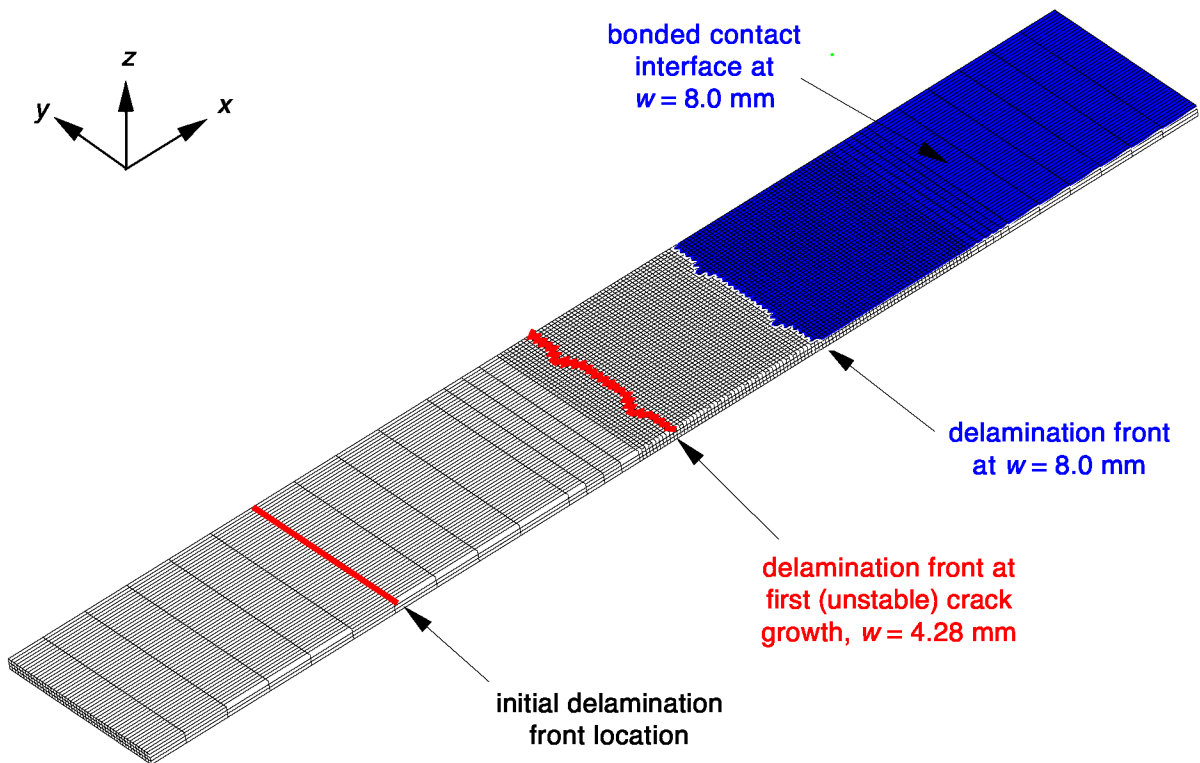


Figure 25. ENF bottom sublaminates mesh with delamination front progression.

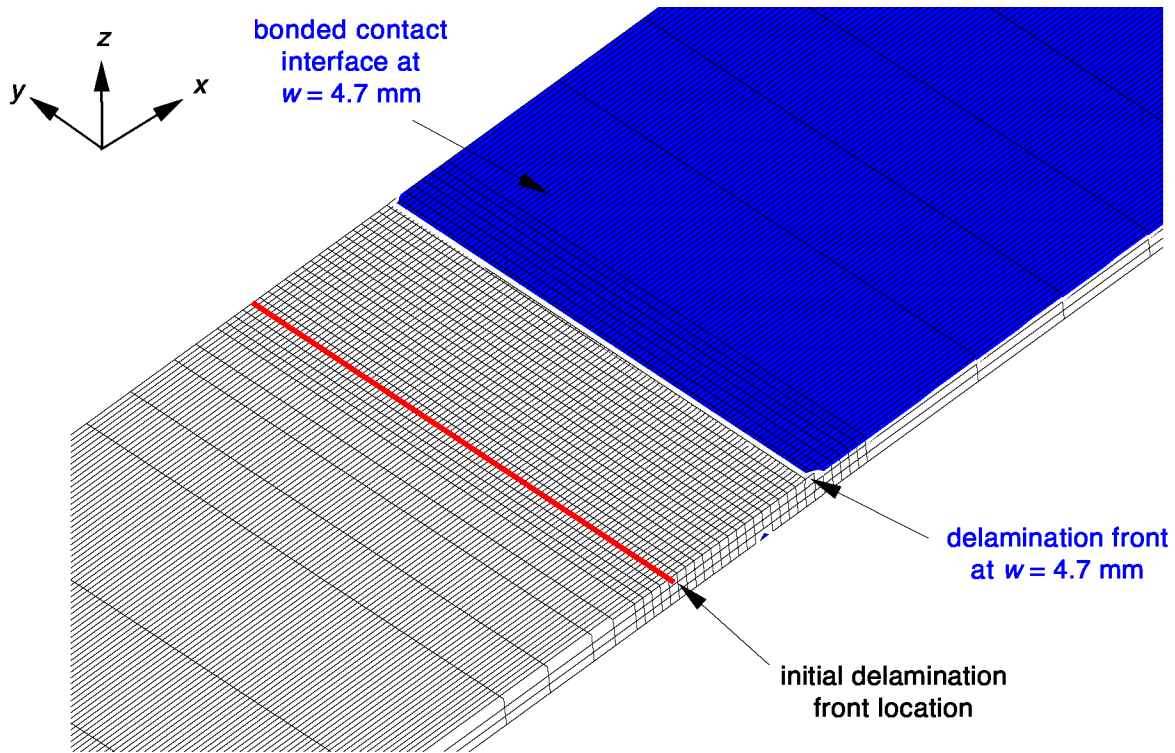


Figure 26. ENF refined model bottom sublaminates mesh with delamination front progression.

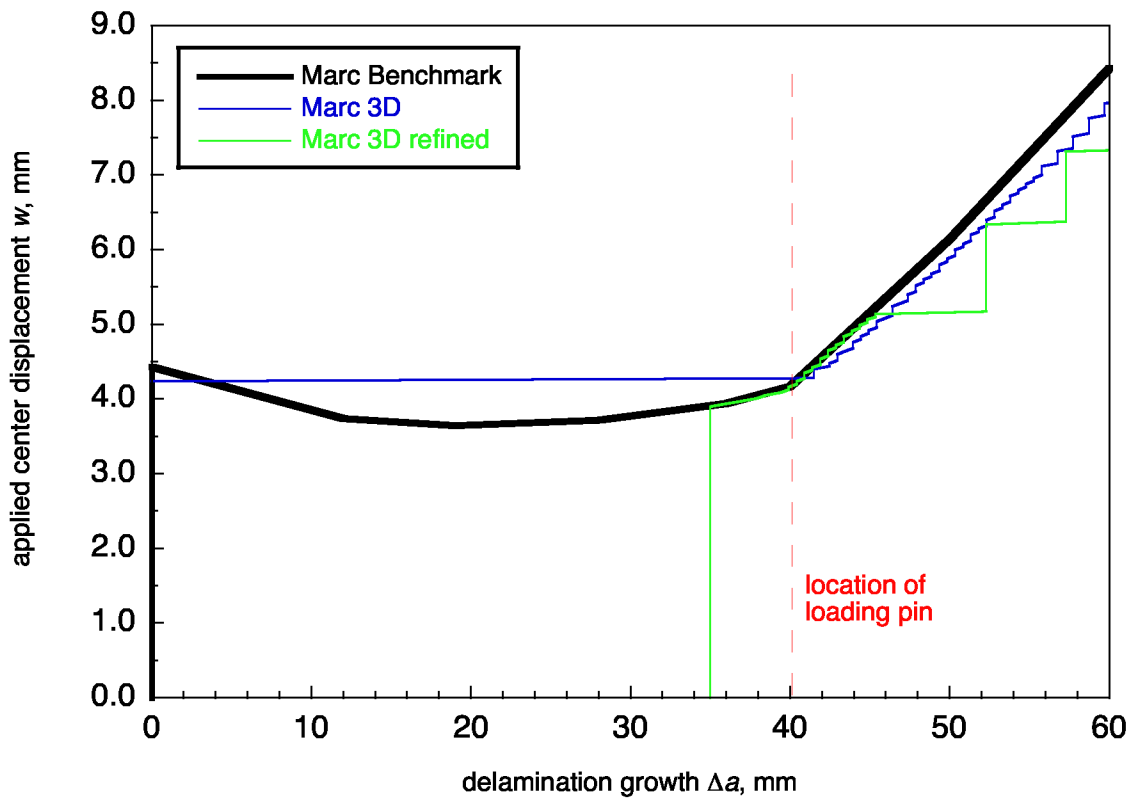


Figure 27. ENF, applied displacement versus delamination length.

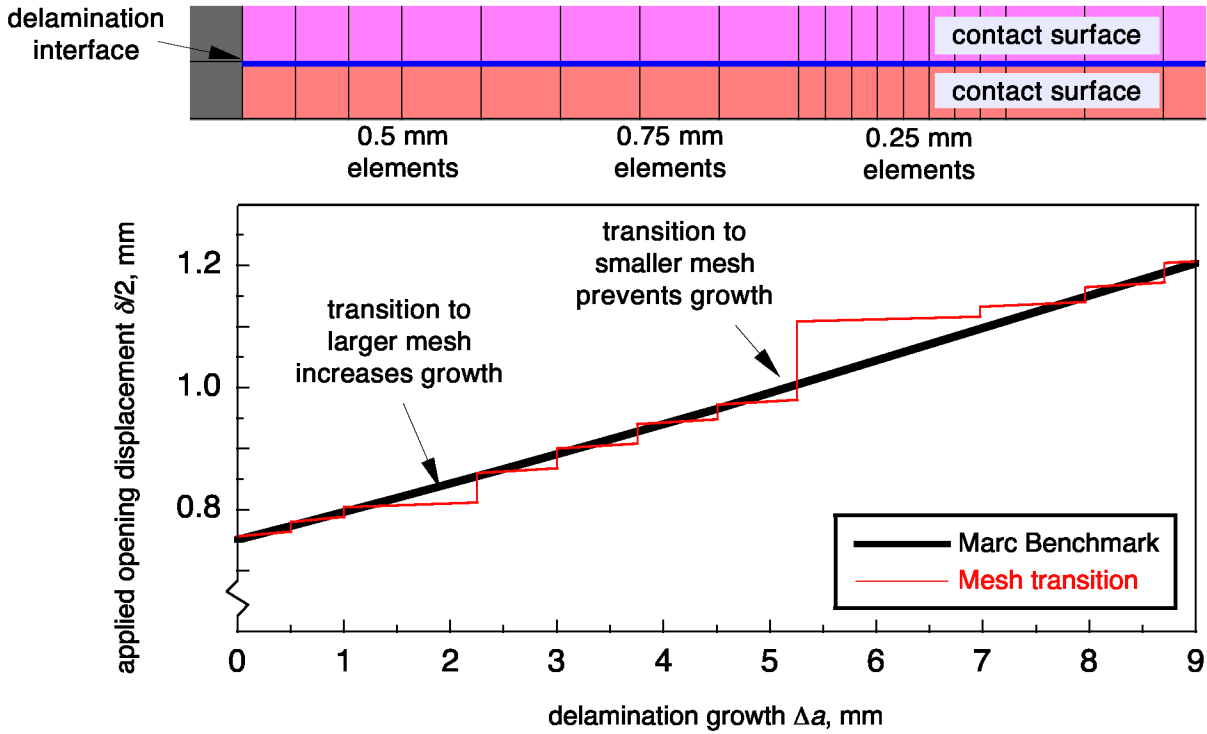


Figure 28. Effect of mesh transition regions, DCB-1 2D.

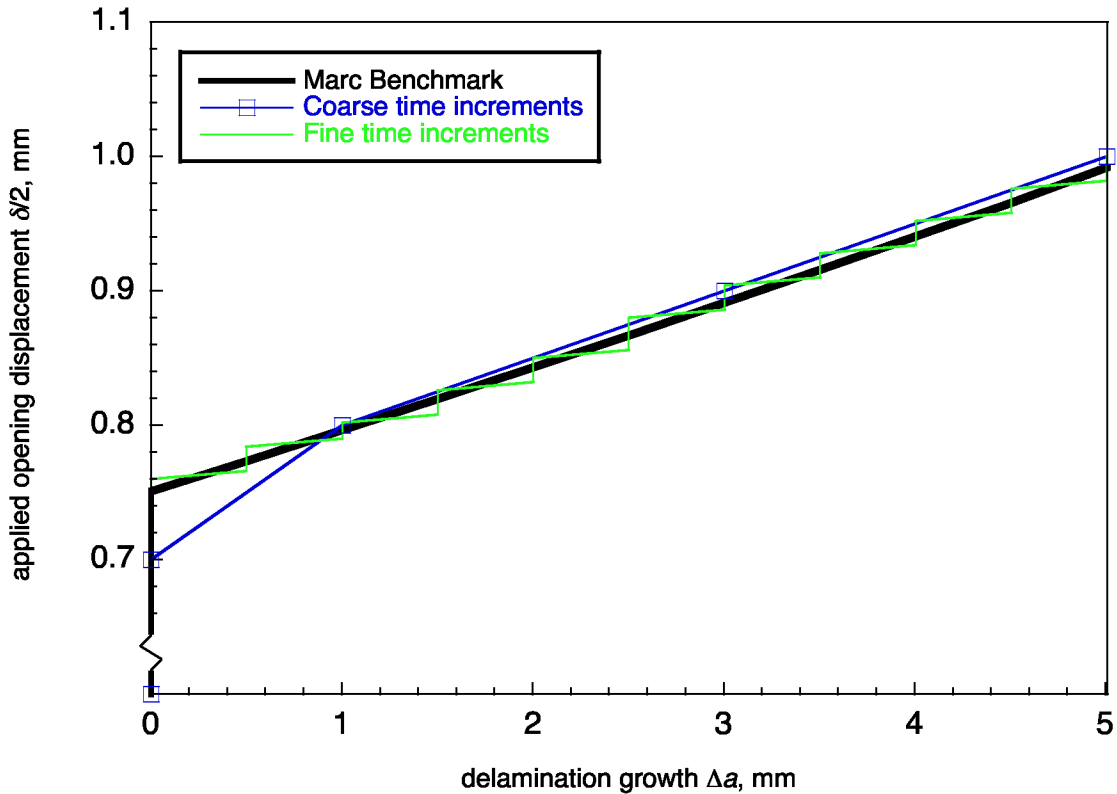


Figure 29. Effect of increment size, DCB-1 2D.

REPORT DOCUMENTATION PAGEForm Approved
OMB No. 0704-0188

The public reporting burden for this collection of information is estimated to average 1 hour per response, including the time for reviewing instructions, searching existing data sources, gathering and maintaining the data needed, and completing and reviewing the collection of information. Send comments regarding this burden estimate or any other aspect of this collection of information, including suggestions for reducing this burden, to Department of Defense, Washington Headquarters Services, Directorate for Information Operations and Reports (0704-0188), 1215 Jefferson Davis Highway, Suite 1204, Arlington, VA 22202-4302. Respondents should be aware that notwithstanding any other provision of law, no person shall be subject to any penalty for failing to comply with a collection of information if it does not display a currently valid OMB control number.
PLEASE DO NOT RETURN YOUR FORM TO THE ABOVE ADDRESS.

1. REPORT DATE (DD-MM-YYYY) 01-06-2010			2. REPORT TYPE Contractor Report		3. DATES COVERED (From - To)	
4. TITLE AND SUBTITLE Assessment of Static Delamination Propagation Capabilities in Commercial Finite Element Codes Using Benchmark Analysis					5a. CONTRACT NUMBER	
					5b. GRANT NUMBER NNL09AA00A	
					5c. PROGRAM ELEMENT NUMBER	
6. AUTHOR(S) Orifici, Adrian C.; Krueger, Ronald					5d. PROJECT NUMBER	
					5e. TASK NUMBER	
					5f. WORK UNIT NUMBER 814358.02.01.07	
7. PERFORMING ORGANIZATION NAME(S) AND ADDRESS(ES) NASA Langley Research Center Hampton, VA 23681-2199 National Institute of Aerospace(NIA) 100 Exploration Way Hampton, VA 23666					8. PERFORMING ORGANIZATION REPORT NUMBER NIA Report No. 2010-03	
9. SPONSORING/MONITORING AGENCY NAME(S) AND ADDRESS(ES) National Aeronautics and Space Administration Washington, DC 20546-0001					10. SPONSOR/MONITOR'S ACRONYM(S) NASA	
					11. SPONSOR/MONITOR'S REPORT NUMBER(S) NASA/CR-2010-216709	
12. DISTRIBUTION/AVAILABILITY STATEMENT Unclassified - Unlimited Subject Category 24 Availability: NASA CASI (443) 757-5802						
13. SUPPLEMENTARY NOTES Langley Technical Monitor: Jonathan B. Ransom						
14. ABSTRACT With capabilities for simulating delamination growth in composite materials becoming available, the need for benchmarking and assessing these capabilities is critical. In this study, benchmark analyses were performed to assess the delamination propagation simulation capabilities of the VCCT implementations in Marc™ and MD Nastran™. Benchmark delamination growth results for Double Cantilever Beam, Single Leg Bending and End Notched Flexure specimens were generated using a numerical approach. This numerical approach was developed previously, and involves comparing results from a series of analyses at different delamination lengths to a single analysis with automatic crack propagation. Specimens were analyzed with three-dimensional and two-dimensional models, and compared with previous analyses using Abaqus®. The results demonstrated that the VCCT implementation in Marc™ and MD Nastran™ was capable of accurately replicating the benchmark delamination growth results and that the use of the numerical benchmarks offers advantages over benchmarking using experimental and analytical results.						
15. SUBJECT TERMS Composites; Delamination propagation; Finite element analysis; Fracture mechanics; Virtual crack closure technique						
16. SECURITY CLASSIFICATION OF:			17. LIMITATION OF ABSTRACT	18. NUMBER OF PAGES	19a. NAME OF RESPONSIBLE PERSON	
a. REPORT	b. ABSTRACT	c. THIS PAGE			STI Help Desk (email: help@sti.nasa.gov)	
U	U	U	UU	47	19b. TELEPHONE NUMBER (Include area code) (443) 757-5802	